34th Symposium on Naval Hydrodynamics
Washington, D.C., June 26-July 1, 2022

Turbulent fluid-structure interaction using DNS/LES: numerical methods and applications

S. Anantharamu[1], S. Prajapati[1], and K. Mahesh[1]
([1]Department of Aerospace Engineering and Mechanics, University of Minnesota, USA)

ABSTRACT

The deforming and curved fluid geometries that arise in turbulent fluid-structure interaction (FSI) problems present unique challenges to LES/DNS. This paper addresses these challenges in the context of a canonical turbulent FSI problem: response of an incompressible viscoelastic wall in an incompressible turbulent channel. Sequential coupling approaches inhibit the parallel scaling of two-way coupled solvers. The development of a parallel two-way coupling approach using Steklov-Poincare operator for finite-volume fluid and finite-element solid discretization is discussed in the context of the same FSI problem. Its multiple-program multiple-data implementation is presented. Some preliminary results of the two-way coupled problem are presented. Several factors affect the vibration of, and sound radiated by an elastic plate excited by turbulent flow. The effect of plate boundary conditions, plate material, and Reynolds number is studied for a plate embedded in the bottom wall of a turbulent channel using one-way coupled DNS. DNS/LES simulations with millions and billions of elements can generate terabytes of unsteady volumetric data. A data-intensive methodology developed to uncover the spectral and spatial features of turbulent fluid sources that excite a plate embedded in the bottom wall of a turbulent channel is discussed. Its application on a 100 TB channel 'big' dataset is presented.

INTRODUCTION

Turbulent fluid-structure interactions, i.e., the interaction of a turbulent flow with a flexible structure, arise in several marine engineering problems. This interaction is three-dimensional and unsteady. Large Eddy Simulation (LES) and Direct Numerical Simulation (DNS) based methods are hence attractive approaches. Our in-house LES/DNS solver MPCUGLES has been extensively used to study turbulent flows in several stationary complex geometries, for e.g., Mahesh et al. (2004); Jang et al. (2012); Kumar and Mahesh (2017). The deforming and curved fluid geometry in turbulent FSI problems presents unique challenges to LES numerics.

The motion performed to adapt the mesh to the changing fluid-solid interface can yield non-planar faces that need to be rectified. For e.g., consider the mesh motion in figure 1a. A corner node of the hexahedral element is moved to account for the deforming geometry. This movement transforms the initially planar face (in red) into a non-planar face, and the new element is no longer a hexahedron. We rectify this issue by discretizing the domain with quadratic hexahedral elements instead. The application of the same mesh motion on a quadratic hexahedral element is shown in figure 1b, and note that the transformed element remains a quadratic hexahedron. Another advantage of the quadratic hexahedron is that it allows for a better representation of curved boundaries that might arise from the small scale solid deformation compared to linear elements. The numerical schemes used for LES need to be non-dissipative. Otherwise, the high-frequency fluctuations will have low energy content (Mittal and Moin, 1997), and the results might not display proper Reynolds number sensitivity. To ensure simulation stability at high Reynolds number with non-dissipative schemes, discrete energy conservation should be enforced. One way to do this in the finite-volume context is to use the equal weight face-interpolation scheme in the convection term (Mahesh et al., 2004). This scheme is second-order on uniform meshes and its accuracy reduces on non-uniform meshes. Therefore, finite-volume LES grids usually have small ($< 2\%$) stretching factor in non-uniform regions to minimize this error. Another feature of finite-volume LES grids is small mesh skewness. In FSI problems, these aspects of the mesh are hard to control because the mesh deforms at every timestep, and therefore, special strategies are necessary to handle situations with large non-uniformity and skewness. This paper discusses some recently developed extensions to the MPCUGLES algorithm to address these issues in the context of a canonical turbulent FSI problem: response of an incompressible viscoelastic

wall in an incompressible turbulent channel.

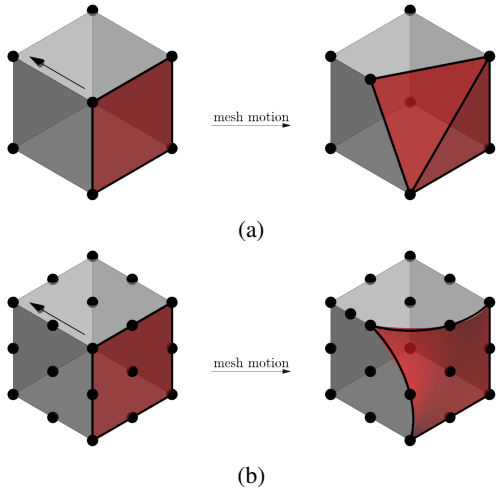

Figure 1: (a) Example mesh motion that transforms the initially planar face (shaded in red) of the linear hexahedron, becoming non-planar. (b) Same mesh motion of figure (a) on a quadratic hexahedron.

Most existing two-way coupling algorithms for finite volume fluid and finite element solid discretization require sequential execution of the fluid and solid solvers, i.e., the two solvers need to be executed one after another and not simultaneously. For e.g., Farhat et al. (1995); Piperno et al. (1995); Piperno and Farhat (2001); Farhat et al. (2006); Degroote et al. (2009); one exception is the vectorial fixed-point algorithm of Mehl et al. (2016). For large scale problems, the sequential execution can become a bottleneck inhibiting the parallel scaling of the coupled solver. Instead, for good parallel scaling, a two-coupling algorithm that allows for simultaneous execution of the two solvers is desired. This paper discusses the development of one such parallel two-way coupling algorithm in the context of the same turbulent FSI problem: response of an incompressible viscoelastic wall in an incompressible turbulent channel. The algorithm couples the finite volume fluid and finite element solid solvers using a scheme based on the Steklov-Poincare operator (Quarteroni and Valli, 1991). Given a boundary value problem, this operator maps the Dirichlet boundary data to the equivalent Neumann boundary data for which the interior solution remains unchanged. Steklov-Poincare based approaches have been developed and previously thought to be possible only for finite element discretization in both fluid and solid domains (Deparis et al., 2006). Ours is the first attempt to extend its applicability to different discretization in the fluid and the solid domain.

The considered turbulent FSI problem has a peculiar solvability requirement. The fluid is incompressible and the fluid subproblem is formulated using only Dirichlet/periodic boundary conditions. Therefore, the pressure in the fluid domain is determinable only up to a constant. This constant is an additional unknown in the problem and needs to be constrained by physically determined equations. Otherwise, the computed solid response would practically be useless. It turns out that the incompressibility condition in the viscoelastic solid supplies these additional constraints. These constraints are: i) the integrated flux of the velocity at the fluid-solid interface should discretely be zero, and ii) the integrated pressure within the fluid and solid should discretely sum to zero. Without enforcing these constraints, the coupled problem cannot be solved. Our method can incorporate these constraints while retaining the parallel coupling aspect. We are not aware of any existing parallel coupling strategies that could incorporate such constraints with finite volume fluid and finite element solid solvers.

Table 1: MPCUGLES-SOLID.

Unified implementation		
	Continuous Galerkin FEM	Mixed FEM
Problems	Comp. elasticity: Dynamic Comp. elasticity: Eigenvalue Comp. elasticity: Static Poisson: Steady	Incomp. viscoelasticity: Dynamic Incomp. viscoelasticity: Eigenvalue Incomp. viscoelasticity: Static
Unknowns storage	Node (d)	(Node (d),Elements (p))
Elements	Quad2d-4node Quad2d-9node Hex3d-8node Hex3d-27node	(Quad2d-9node,Tri2d-global-disc) (Hex3d-27node,Tet3d-global-disc)
Matrix prob.	$K_{eff}d = f$	$K_{eff}d + Gp = b_d$ $G^T d = b_p$
Part. soft.	`ParMETIS`	`ParMETIS`
LA solver: in-house	CG Flexible GMRES	Flexible GMRES
LA solver: TPL	Krylov subspace (`Belos`) Sparse LU (`SuperLU_DIST`)	Krylov subspace (`Belos`)
Prec.: in-house	Scaled thickness prec.	Stokes upper tridiagonal Sylvester, Elman, Kay & Wathen
Prec.: TPL	AMG (`MueLu`) IChol (`Ifpack2`)	ILU (`Ifpack2`)
Eig. solver: TPL	LOBPCG-AMG (`Anasazi`)	Block Krylov Schur (`Anasazi`)
I/O: Raw	`PnetCDF`	`PnetCDF`
I/O: Vis.	`Exodus`	`Exodus`

The small length and time scales of the turbulent

fluid stresses can yield unsteady solid deformation of comparable length and time scales, especially for a soft solid material. The solid sub-domain solver should be able to handle the large number of degrees of freedom required to resolve this small-scale deformation. Different solid materials require different numerical methods for their efficient solution. A compressible solid material, for e.g., steel and aluminum, requires the continuous Galerkin finite element method (FEM) which stores unknowns at the nodes, whereas, an incompressible solid material, for e.g., polydimethylsiloxane requires the mixed FEM which stores unknowns at both nodes and inside elements. Without data structures that enable unified implementation of both these methods, code development would be inefficient. Our in-house parallel code `MPCUGLES-SOLID` (Anantharamu and Mahesh, 2021) provides a unified implementation of both continuous Galerkin FEM and mixed FEM through specially designed data structures. The code can solve static, dynamic, and eigenvalue problems. For interprocessor communication, it uses message-passing modules which have been tested up to 100,000 processors. For efficient solution of massively large problems, the solver provides several linear algebra solver and preconditioner options through both in-house implementations and third-party libraries such as `Trilinos` (Trilinos Project Team) and `SUPERLU_DIST` (Li and Demmel, 2003). Table 1 summarizes the key features of `MPCUGLES-SOLID`.

The vibration and sound radiated by a plate excited by turbulent wall-pressure fluctuations depends on several factors including plate boundary condition, plate material, and Reynolds number. Most previous theoretical and numerical studies (Hwang and Maidanik, 1990; Blake, 2017; Hambric et al., 2004; Esmailzadeh et al., 2009; De Rosa and Franco, 2008) to understand this dependence used wall-pressure models (Corcos, 1964; Chase, 1980, 1987; Smol'Iakov and Tkachenko, 1991; Mellen, 1994; Goody, 2004; Bull, 1967). Advances in high-performance computing now allow us to directly compute the unsteady turbulent wall-pressure fluctuations at moderate Reynolds numbers using DNS. We use these time-domain DNS wall-pressure fluctuations to study this dependence instead. This study assumes the coupling to be one-way, i.e., the turbulent flow affects the plate and not vice versa. For vibrations of small amplitude, one-way coupling is widely accepted to be sufficient. By small, we mean the displacement and the velocity to be smaller than the viscous units. All previously mentioned wall-pressure model-based studies use the one-way coupled approximation.

Turbulent simulations using DNS/LES yield unsteady and three-dimensional velocity and pressure fields. Advances in parallel I/O now allow us to store and process terabytes of this data to answer some fundamental questions in a reasonable amount of time. We discuss our one such 'big data' effort in the context of turbulent FSI. A methodology (Anantharamu and Mahesh, 2021) to identify the frequency-dependent wall-normal distribution of turbulent sources that excite a plate at the bottom wall of a channel is presented and applied to a 100 TB channel DNS dataset.

The paper is organized as follows. Section Fluid DNS/LES methodology discusses the MPCUGLES extensions to curved and deforming gometries. An implementation within MPCUGLES-SOLID to simulate incompressible viscoelastic materials is discussed in section Viscoelastic implementation in MPCUGLES-SOLID. In section Two-way coupling, we present some results of the two-way coupled problem using the sequential fixed-point iteration and discuss the development of the proposed two-way parallel coupling method based on the Steklov-Poincare operator. New findings on the effect of plate boundary condition, plate material and Reynolds number on turbulent wall-pressure induced plate vibration and far-field sound radiation is discussed in section one-way coupled plate excitation. Section One-way coupled plate excitation source analysis discusses the analysis of plate excitation sources using the channel DNS dataset. The paper is summarized in section Summary.

FLUID DNS/LES METHODOLOGY

Method

The incompressible Navier-Stokes equations in the Arbitrary Lagrangian Eulerian (ALE) frame of reference are:

$$\begin{aligned} &\frac{d\mathbf{u}(\mathbf{x}_g(t),t)}{dt} - \mathbf{v}_\mathrm{g}\cdot\boldsymbol{\nabla}\mathbf{u} + \boldsymbol{\nabla}\cdot\left(\mathbf{u}\mathbf{u}^\mathrm{T}\right) = \\ &-\boldsymbol{\nabla}p + \nu\boldsymbol{\nabla}^2\mathbf{u} + \boldsymbol{\ell} \text{ in } \Omega(t), \\ &\boldsymbol{\nabla}\cdot\mathbf{u} = 0 \text{ in } \Omega(t). \end{aligned} \tag{1}$$

Here, $\mathbf{u}$ is the fluid velocity vector, p is the fluid pressure, ν is the kinematic viscosity, $\boldsymbol{\ell}$ is the body force vector, $\mathbf{x}_g(t)$ is the mesh trajectory, $\mathbf{v}_\mathrm{g}$ is the mesh velocity, and $\Omega(t)$ is the deforming curved geometry. For LES, the velocity and pressure are interpreted to be their filtered counterparts, and the term $\nu\boldsymbol{\nabla}^2\mathbf{u}$ is replaced by $(\boldsymbol{\nabla}\cdot[(\nu+\nu_T)\boldsymbol{\nabla}\mathbf{u}])$, where ν_T is the subgrid-scale viscosity computed using the subgrid-scale model.

To construct a spatially second-order, non-dissipative, energy conserving scheme, we map the curved and deforming geometry at each timestep to a uniform structured grid using quadratic hexahedral finite elements. At each time t, this mapping denoted by $\boldsymbol{\varphi}$ relates each coordinate vector $\mathbf{X}$ in the uniform structured grid domain $\widehat{\Omega}$ to a coordinate vector $\mathbf{x}$ in the discrete current domain $\Omega_h(t)$, i.e., $\mathbf{x} = \boldsymbol{\varphi}(\mathbf{X},t)$. Figure 2 shows a schematic of

the mapping. Note that we refer to the uniform structured grid domain as the 'reference domain' and the discrete current domain as just the 'current domain'. To construct the mapping, the coordinate vector of each node in the reference domain is first assigned and then interpolated to the interior of the reference domain elements using quadratic shape functions. The node coordinate of node 'ino' at time t is denoted by $\boldsymbol{\varphi}_{\text{ino}}(t)$, and inside each element we have

$$\boldsymbol{\varphi}(\mathbf{X},t) = \sum_{\text{nodes}} \boldsymbol{\varphi}_{\text{ino}}(t) N_{\text{ino}}(\mathbf{X}), \tag{2}$$

where $N_{\text{ino}}(\mathbf{X})$ is the quadratic shape function corresponding to node 'ino'. In FSI problems, a mesh motion algorithm is required to set $\boldsymbol{\varphi}_{\text{ino}}(t)$ from the coordinates of the fluid-solid interface. We use the Laplacian extension approach of Nobile (2001). In problems where the deformation of the fluid geometry is known apriori, the node coordinates can simply be prescribed.

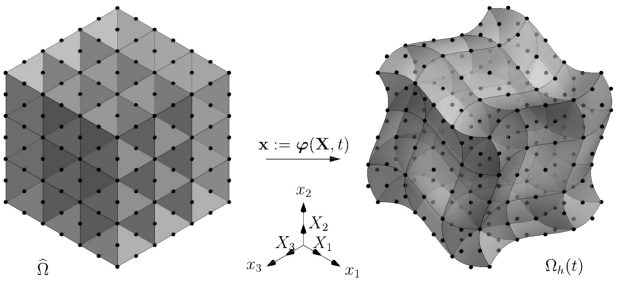

Figure 2: Schematic of the mapping $\boldsymbol{\varphi}$.

The method is derived as follows. Integrate equation 1 over each quadratic hexahedral element 'cv' in the current domain to obtain,

$$\begin{aligned}
&\frac{d}{dt}\int_{\Omega_{\text{cv}}(t)} \mathbf{u}(\mathbf{x}_g(t),t)\, d\Omega + \int_{\Omega_{\text{cv}}(t)} \boldsymbol{\nabla}\cdot\left(\mathbf{u}(\mathbf{u}-\mathbf{v}_{\text{g}})^{\text{T}}\right)\, d\Omega = \\
&-\int_{\Omega_{\text{cv}}(t)} \boldsymbol{\nabla} p\, d\Omega + \int_{\Omega_{\text{cv}}(t)} \nu\boldsymbol{\nabla}^2\mathbf{u}\, d\Omega + \int_{\Omega_{\text{cv}}(t)} \boldsymbol{\ell}\, d\Omega, \\
&\int_{\Omega_{\text{cv}}(t)} \boldsymbol{\nabla}\cdot\mathbf{u}\, d\Omega = 0.
\end{aligned} \tag{3}$$

In the above equation, a manipulation (Donea et al., 2017) is performed to pull the spatial integral inside the temporal integral in the first term. A requirement to discretely preserve the freestream condition under arbitrary mesh motion is to solve the Discrete Geometric Conservation Law (DGCL) (Thomas and Lombard, 1979) in addition to the above governing equations. The DGCL equation is

$$\frac{d}{dt}\int_{\Omega_{\text{cv}}(t)} 1\, d\Omega = \int_{\Omega_{\text{cv}}(t)} \boldsymbol{\nabla}\cdot\mathbf{v}_{\text{g}}\, d\Omega. \tag{4}$$

Transform the integrals in equations 3 and 4 to the equivalent integrals in the reference domain.

$$\begin{aligned}
&\int_{\widehat{\Omega}_{\text{cv}}} \frac{\partial}{\partial t}\left(\mathbf{U}J\right)\, d\widehat{\Omega} + \int_{\widehat{\Omega}_{\text{cv}}} \boldsymbol{\nabla}_{\mathbf{X}}\cdot\left(\mathbf{U}\left[J\mathbf{F}^{-1}(\mathbf{U}-\mathbf{V}_{\text{g}})\right]^{\text{T}}\right)\, d\widehat{\Omega} = \\
&-\int_{\widehat{\Omega}_{\text{cv}}} \boldsymbol{\nabla}_{\mathbf{X}}\cdot\left(PJ\mathbf{F}^{-\text{T}}\right)\, d\widehat{\Omega} + \\
&\int_{\widehat{\Omega}_{\text{cv}}} \nu\boldsymbol{\nabla}_{\mathbf{X}}\cdot\left(\left[\left(\boldsymbol{\nabla}_{\mathbf{X}}\mathbf{U}\right)\mathbf{F}^{-1}\right]J\mathbf{F}^{-\text{T}}\right)\, d\widehat{\Omega} + \int_{\widehat{\Omega}_{\text{cv}}} J\mathbf{L}\, d\widehat{\Omega}, \\
&\int_{\widehat{\Omega}_{\text{cv}}} \boldsymbol{\nabla}_{\mathbf{X}}\cdot\left(J\mathbf{F}^{-1}\mathbf{U}\right)\, d\widehat{\Omega} = 0, \\
&\int_{\widehat{\Omega}_{\text{cv}}} \frac{\partial J}{\partial t}\, d\widehat{\Omega} = \int_{\widehat{\Omega}_{\text{cv}}} \boldsymbol{\nabla}_{\mathbf{X}}\cdot\left(J\mathbf{F}^{-1}\mathbf{V}_{\text{g}}\right)\, d\widehat{\Omega}.
\end{aligned} \tag{5}$$

Here, $\widehat{\Omega}_{\text{cv}}$ is the corresponding quadratic hexahedral element in the reference domain. The uppercase variables $\mathbf{U}, P, \mathbf{V}_{\text{g}}, \mathbf{L}$ relate to their lowercase counterparts via the mapping $\boldsymbol{\varphi}$, for e.g., $\mathbf{U}(\mathbf{X},t) = \mathbf{u}(\boldsymbol{\varphi}(\mathbf{X},t),t)$. $\boldsymbol{\nabla}_{\mathbf{X}}$ denotes the gradient along coordinate directions in the reference domain. $\mathbf{F}$ is the Jacobian matrix of $\boldsymbol{\varphi}$. Its $(i,j)^{th}$ component, F_{ij}, is $\partial\varphi_i/\partial X_j$. J is the determinant of the Jacobian matrix, i.e., $J = \det(\mathbf{F})$.

A predictor-corrector method is used to integrate equation 5 in time. In the predictor step, the DGCL equation and the momentum equations without the pressure gradient term are advanced in time using the explicit Adams-Bashforth scheme.

$$\begin{aligned}
&\int_{\widehat{\Omega}_{\text{cv}}} \frac{\widetilde{J}^{n+1}-\widetilde{J}^{n}}{\Delta t}\, d\widehat{\Omega} = \sum_{\text{faces of cv}} \left(\frac{3}{2}\text{GVEL}^{n}_{\text{face}} - \frac{1}{2}\text{GVEL}^{n-1}_{\text{face}}\right)\widehat{A}_{\text{face}}, \\
&\int_{\widehat{\Omega}_{\text{cv}}} \frac{\widehat{\mathbf{U}}\widetilde{J}^{n+1}-\mathbf{U}^{n}\widetilde{J}^{n}}{\Delta t}\, d\widehat{\Omega} = \sum_{\text{faces of cv}} \left(\frac{3}{2}\left[-\mathbf{NL}^{n}_{\text{face}} + \mathbf{VISC}^{n}_{\text{face}}\right]\right. \\
&\left. -\frac{1}{2}\left[-\mathbf{NL}^{n-1}_{\text{face}} + \mathbf{VISC}^{n-1}_{\text{face}}\right]\right)\widehat{A}_{\text{face}} + \\
&\int_{\widehat{\Omega}_{\text{cv}}} \left(\frac{3}{2}J^{n}\mathbf{L}^{n} - \frac{1}{2}J^{n-1}\mathbf{L}^{n-1}\right)\, d\widehat{\Omega}.
\end{aligned} \tag{6}$$

Here, the fluxes $\text{GVEL}^{n}_{\text{face}}$, $\mathbf{NL}^{n}_{\text{face}}$, and $\mathbf{VISC}^{n}_{\text{face}}$ are defined to be

$$\begin{aligned}
\text{GVEL}^{n}_{\text{face}} &= \left(\int_{\text{face}} \left(J^{n}\mathbf{F}^{n^{-1}}\mathbf{V}^{n}_{\text{g}}\right)\cdot\mathbf{N}\, d\widehat{\Gamma}\right)/\widehat{A}_{\text{face}} \\
\mathbf{NL}^{n}_{\text{face}} &= \left(\int_{\text{face}} \mathbf{U}^{n}\left(\left[J^{n}\mathbf{F}^{n^{-1}}\left(\mathbf{U}^{n}-\mathbf{V}^{n}_{\text{g}}\right)\right]\cdot\mathbf{N}\right) d\widehat{\Gamma}\right)/\widehat{A}_{\text{face}} \\
\mathbf{VISC}^{n}_{\text{face}} &= \left(\int_{\text{face}} \nu\left[J^{n}\mathbf{F}^{n^{-1}}\left(\mathbf{F}^{n^{-\text{T}}}\left[\boldsymbol{\nabla}_{\mathbf{X}}\mathbf{U}^{n}\right]^{\text{T}}\right)\right]\cdot\mathbf{N}\, d\widehat{\Gamma}\right)/\widehat{A}_{\text{face}}
\end{aligned} \tag{7}$$

In the corrector step, a Poisson equation for the pressure is solved and the predicted velocity is corrected to be divergence-free.

$$\begin{aligned}
&-\sum_{\text{faces of cv}} \text{GP}^{n+1}_{\text{face}}\widehat{A}_{\text{face}} = \\
&-\frac{1}{\Delta t}\sum_{\text{faces of cv}} \int_{\text{face}} \left(J^{n+1}\mathbf{F}^{n+1^{-1}}\widehat{\mathbf{U}}\right)\cdot\mathbf{N}\, d\widehat{\Gamma}, \\
&\int_{\widehat{\Omega}_{\text{cv}}} \frac{\mathbf{U}^{n+1}J^{n+1}-\widehat{\mathbf{U}}J^{n+1}}{\Delta t}\, d\widehat{\Omega} = \\
&-\int_{\widehat{\Omega}_{\text{cv}}} \boldsymbol{\nabla}_{\mathbf{X}}\cdot\left(P^{n+1}J^{n+1}\mathbf{F}^{n+1^{-\text{T}}}\right)\, d\widehat{\Omega}.
\end{aligned} \tag{8}$$

where $\text{GP}_{\text{face}}^{n+1}$ is the flux of the pressure gradient at the face, and it is defined as

$$\text{GP}_{\text{face}}^{n} = \left(\int_{\text{face}} \left[J^n \mathbf{F}^{n^{-1}} \left(\mathbf{F}^{n^{-\text{T}}} \boldsymbol{\nabla}_{\mathbf{X}} P^n \right) \right] \cdot \mathbf{N} \, \mathrm{d}\widehat{\Gamma} \right) / \widehat{A}_{\text{face}} \quad (9)$$

A variable storage similar to Mahesh et al. (2004) is used. The variables $\widetilde{J}^n$, $\mathbf{U}^n$, and P^n are stored at the centroid of each reference quadratic hexahedral element. A face-averaged normal velocity $V_{\text{N,face}}^n$ defined as $\left[\int_{\text{face}} \left(J^n \mathbf{F}^{-1^n} \mathbf{U}^n \right) \cdot \mathbf{N} \, d\widehat{\Gamma} \right] / \widehat{A}_{\text{face}}$ is stored at each face and advanced separately. Using this storage, the individual terms in equations 6 and 8 are approximated as follows. The unsteady terms in the DGCL, predictor and corrector equations are approximated using the cell-centroid values as

$$\begin{aligned}
\int_{\widehat{\Omega}_{\text{cv}}} \frac{\widetilde{J}^{n+1} - \widetilde{J}^n}{\Delta t} \, d\widehat{\Omega} &\approx \frac{\widetilde{J}_{\text{cv}}^{n+1} - \widetilde{J}_{\text{cv}}^n}{\Delta t} |\widehat{\Omega}_{\text{cv}}|, \\
\int_{\widehat{\Omega}_{\text{cv}}} \frac{\widehat{\mathbf{U}} \widetilde{J}^{n+1} - \mathbf{U}^n \widetilde{J}^n}{\Delta t} \, d\widehat{\Omega} &\approx \frac{\widehat{\mathbf{U}}_{\text{cv}} \widetilde{J}_{\text{cv}}^{n+1} - \mathbf{U}_{\text{cv}}^n \widetilde{J}_{\text{cv}}^n}{\Delta t} |\widehat{\Omega}_{\text{cv}}|, \text{ and} \\
\int_{\widehat{\Omega}_{\text{cv}}} \frac{\mathbf{U}^{n+1} J^{n+1} - \widehat{\mathbf{U}} J^{n+1}}{\Delta t} \, d\widehat{\Omega} &\approx \frac{\mathbf{U}_{\text{cv}}^{n+1} - \widehat{\mathbf{U}}_{\text{cv}}}{\Delta t} |\Omega_{\text{cv}}^{n+1}|,
\end{aligned} \quad (10)$$

where $|\widehat{\Omega}_{\text{cv}}|$ and $|\Omega_{\text{cv}}^{n+1}|$ are the volumes of the quadratic hexahedral element in the reference and current domain at timestep $n+1$, respectively. $\text{GVEL}_{\text{face}}^n$ is computed exactly using Gauss quadrature. The fluxes $\mathbf{NL}_{\text{face}}^n$, $\mathbf{VISC}_{\text{face}}^n$, and $\text{GP}_{\text{face}}^n$ are approximated as

$$\begin{aligned}
\mathbf{NL}_{\text{face}}^n &\approx \frac{1}{2} \left(\mathbf{U}_{\text{cv}}^n + \mathbf{U}_{\text{nbr}}^n \right) \left(V_{\text{N,face}}^n - \text{GVEL}_{\text{face}}^n \right), \\
\mathbf{VISC}_{\text{face}}^n &\approx \nu_{\text{face}} \left(\left[\mathbf{F}^n \right]_{\text{face}}^{-\text{T}} \left[\mathbf{D}_{\mathbf{X}} \, \mathbf{U}^n \right]_{\text{face}}^{\text{T}} \right) \cdot \frac{\left[\int_{\text{face}} J^n \mathbf{F}^{n^{-\text{T}}} \mathbf{N} \, \mathrm{d}\widehat{\Gamma} \right]}{\widehat{A}_{\text{face}}}, \\
\text{GP}_{\text{face}}^n &\approx \left[\left[\mathbf{F}^n \right]_{\text{face}}^{-\text{T}} \left[\mathbf{D}_{\mathbf{X}} \, P^n \right]_{\text{face}} \right] \cdot \frac{\left[\int_{\text{face}} J^n \mathbf{F}^{n^{-\text{T}}} \mathbf{N} \, \mathrm{d}\widehat{\Gamma} \right]}{\widehat{A}_{\text{face}}}.
\end{aligned} \quad (11)$$

Here, $\left[\mathbf{D}_{\mathbf{X}} \, \mathbf{U}^n \right]_{\text{face}}$ and $\left[\mathbf{D}_{\mathbf{X}} \, P^n \right]_{\text{face}}$ are the second-order accurate approximation to the derivatives of velocity and pressure, respectively, at the face-centroids. These are constructed using the cell-centered values. $V_{\text{N,face}}^n$ is the approximation to the face-normal velocity which is time-advanced separately. The face-averaged normal $\left[\int_{\text{face}} J^n \mathbf{F}^{n^{-\text{T}}} \mathbf{N} \, \mathrm{d}\widehat{\Gamma} \right] / \widehat{A}_{\text{face}}$ is computed exactly using Gauss quadrature. In equation 8, the flux of the predicted velocity is approximated as

$$\int_{\text{face}} \left(J^{n+1} \mathbf{F}^{n+1^{-1}} \widehat{\mathbf{U}} \right) \cdot \mathbf{N} \, d\widehat{\Gamma} \approx \widehat{V}_{\text{N,face}} \widehat{A}_{\text{face}}, \quad (12)$$

where $\widehat{V}_{\text{N,face}}$ is defined as

$$\frac{\left(\widehat{\mathbf{U}}_{\text{cv}} + \widehat{\mathbf{U}}_{\text{nbr}} \right)}{2} \cdot \frac{\left[\int_{\text{face}} J^n \mathbf{F}^{n^{-\text{T}}} \mathbf{N} \, \mathrm{d}\widehat{\Gamma} \right]}{\widehat{A}_{\text{face}}},$$

and the volume integral of pressure gradient is reconstructed as

$$\begin{aligned}
&\int_{\widehat{\Omega}_{\text{cv}}} \boldsymbol{\nabla}_{\mathbf{X}} \cdot \left(P^{n+1} J^{n+1} \mathbf{F}^{n+1^{-\text{T}}} \right) \, d\widehat{\Omega} \approx \\
&|\Omega_{\text{cv}}^{n+1}| \frac{\mathbf{F}_{\text{cv}}^{n+1}}{J_{\text{cv}}^{n+1}} \sum_{\text{faces of icv}} \frac{\mathbf{N}_{\text{face}}}{2} \text{GP}_{\text{face}}^{n+1}.
\end{aligned} \quad (13)$$

Finally, the face-averaged normal velocity is advanced as

$$V_{\text{N,face}}^{n+1} = \widehat{V}_{\text{N,face}} - \Delta t \, \text{GP}_{\text{face}}^n$$

Brief remarks follow. The method is spatially second-order accurate, irrespective of mesh skewness, and non-uniformity. The convective discretization is non-dissipative, conserves kinetic energy discretely, and ensures freestream preservation on curved meshes. The cell-centered pressure gradient reconstruction scheme in equation 13 is novel. Tests on a Poisson problem showed that this scheme is second-order accurate irrespective of the boundary condition, while the commonly used Green-Gauss reconstruction scheme can become first-order in the presence of Dirichlet/Neumann boundary conditions.

Preconditioning

The pressure Poisson equation consumes bulk of the solver time, and therefore, an efficient preconditioner for its iterative solution is crucial for good parallel scaling. This need is amplified for FSI problems because the pressure Poisson equation is solved multiple times within a timestep. With the above discretization of the pressure gradient flux, the obtained 27-point stencil Poisson matrix can be non-symmetric. Hence, existing state-of-the-art techniques such as the multigrid preconditioned conjugate gradient (CG) solver cannot be directly used for its solution. We propose to use flexible GMRES (Saad, 2003) as the solver and a few multigrid preconditioned CG iterations on the symmetric 7-pt stencil Poisson matrix as the preconditioner. The CG iterations in the preconditioner are performed until an approximate solution with a larger residual is obtained.

For Dirichlet/periodic boundary conditions on the velocity, the pressure Poisson equation has a non-zero null vector – the vector of ones. This null vector should be incorporated in the following manner within the flexible GMRES iterations; otherwise, the iterations were found to stagnate. At the beginning of each iteration, the matrix-vector product should be projected orthogonal to the null-vector, and the preconditioner should be applied on this projected vector instead of applying it directly on the matrix-vector product.

To check the optimality of this solution procedure, we solve a 2D periodic Poisson problem on a sinusoidally perturbed mesh for different mesh resolutions, and tabulate the number of GMRES iterations. The right-hand side of the Poisson problem is set by assuming the exact solution to be $\cos(2\pi x_1)\cos(2\pi x_2)$. The

node-coordinates of the perturbed mesh are set using the mapping

$$x_1(\mathbf{X}) = X_1 - \alpha \sin(2\pi X_2), \\ x_2(\mathbf{X}) = X_2 - \alpha \sin(2\pi X_1), \tag{14}$$

and the reference domain is chosen to be a unit square. Figure 3 shows the computed solution with 32 elements along each direction. The number of GMRES iterations for each mesh resolution is tabulated in the second column of table 2. Note that for the preconditioner, we use the CG and the multigrid implementations within the Belos and MueLu package of Trilinos (Trilinos Project Team), respectively. The tolerances used on the preconditioner and GMRES iterations are 10^{-2} and 10^{-8}, respectively. The GMRES iteration count is found to increase only moderately with problem size, and therefore, the solution procedure is optimal. The number of preconditioner CG iterations are shown in the third column of the same table. These iterations also increase moderately with problem, and therefore, the preconditioner cost is also reasonable.

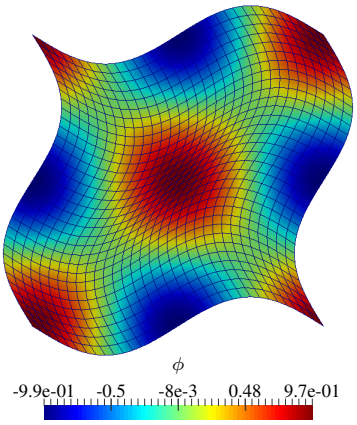

Figure 3: Poisson test case with 32 elements along each direction.

Table 2: Pressure Poisson iteration count

N	Solver iterations	Preconditioner iterations
32	18	2.2
64	23	2.3
128	26	3.3
256	26	5.5
512	25	8.6

In deforming geometries, the pressure Poisson coefficients change at each timestep. The cost of recomputing the multigrid auxillary data at each timestep is high. To reduce this cost, we instead recompute this auxiliary data every $N_{p,t}$ timesteps. For a good choice of $N_{p,t}$, the number of GMRES iterations was found to be similar to that obtained by recomputing the preconditioner at each timestep. The value of $N_{P,t}$ is problem-dependent; for e.g., for the Taylor-Green test case discussed in the below subsection, we set $N_{p,t}$ to 100.

Validation

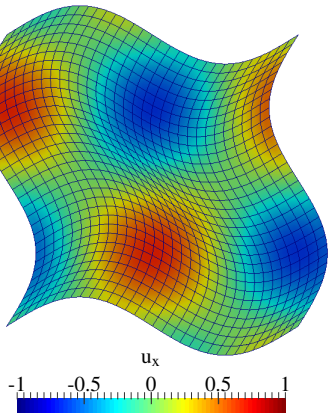

(a) Streamwise velocity for the Taylor-Green problem on a deforming mesh at time $T_g/2$.

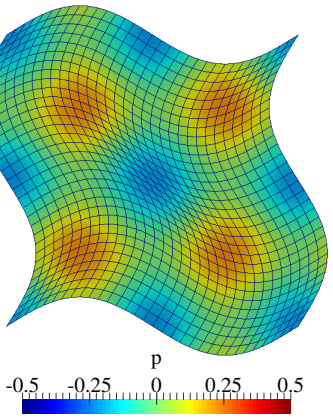

(b) Pressure for the Taylor-Green problem on a deforming mesh at time $T_g/2$.

Mesh	u_1		u_2		p	
N	$error$	$order$	$error$	$order$	$error$	$order$
32	7.9e−3	–	7.9e−3	–	2.4e−2	–
64	2.2e−3	1.84	2.2e−3	1.83	6.6e−3	1.87
128	5.7e−4	1.96	5.7e−4	1.95	1.7e−3	1.96
256	1.4e−4	1.99	1.4e−4	1.99	4.3e−4	1.99
512	3.6e−5	2.00	3.6e−5	2.00	1.1e−4	2.00

Table 3: History of convergence of the cell-centered velocity and pressure for the Taylor-Green problem on a deforming mesh at Reynolds number 100.

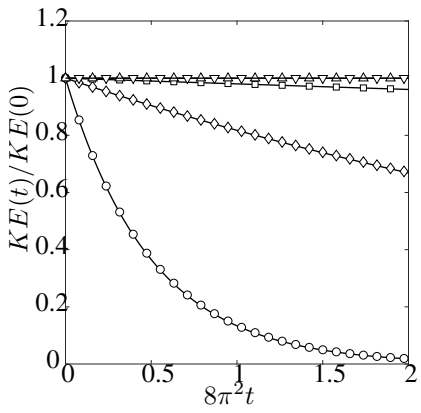

Figure 5: Evolution of discrete kinetic energy for the Taylor-Green problem on a deforming mesh at different Reynolds number. Symbols $\circ$, $\diamond$, $\square$, $\triangle$, and $\triangledown$ denote the analytical decay at Reynolds numbers 1, 10, 10^2, 10^4, and ∞, respectively. Lines denote the computed decay at the corresponding Reynolds number.

The spatial accuracy and discrete energy conservation aspects of our method are demonstrated by solving the periodic Taylor-Green problem on a deforming mesh. The Reynolds numbers considered are 1, 10, 10^2, 10^4, and ∞. The mesh motion is assumed to be

$$\begin{aligned}
\varphi_1(\mathbf{X},t) &= X_1 - \alpha \sin(2\pi X_2)\cos\left(\frac{2\pi}{T_g}t\right), \\
\varphi_2(\mathbf{X},t) &= X_2 - \alpha \sin(2\pi X_1)\cos\left(\frac{2\pi}{T_g}t\right), \\
\varphi_3(\mathbf{X},t) &= X_3,
\end{aligned} \tag{15}$$

where α is the amplitude and T_g is the time period of the oscillation. We choose $\alpha = 0.1$, and $T_g = 1$. $\alpha = 0.1$ ensures the presence of extremely skewed elements. For $T_g = 1$, the grid velocity and the flow velocity are of the same order of magnitude. Figures 4a and 4b and show the streamwise velocity and pressure fields computed with 32 elements in each direction at time $T_g/2$ for Reynolds number 100. The solution is very accurate even though the control volumes become extremely skewed, especially at the corners. Table 3 tabulates the maximum error in the computed cell-centered velocity and pressure with increasing mesh resolution for Reynolds number 100. The error is measured at the end of time $t = 0.025$, and the timestep for each mesh is set to a very small value to isolate only the spatial discretization error. Both cell-centered velocity and pressure converge with second-order accuracy. Figure 5 shows the evolution of discrete kinetic energy with time for all the Reynolds numbers using 32 elements in each direction. The simulation results agree with the analytical results for all Reynolds numbers. The $Re = \infty$ case is stable because our method enforces discrete energy conservation. Formulations that do not enforce such energy conservation, for e.g., interpolating $u_i u_j$ instead of just u_i in the convective-term discretization, can yield unstable solutions for the $Re = \infty$ case (Mahesh et al., 2004).

To demonstrate the freestream preservation aspect of our method, we consider a deforming mesh and advance a constant velocity field with periodic boundary conditions. The deforming mesh considered is (Persson et al., 2009)

$$\begin{aligned}
\varphi_1(\mathbf{X},t) &= \widehat{X}_1(\mathbf{X}) + 2\sin\left(\frac{\pi \widehat{X}_1(\mathbf{X})}{10}\right)\sin\left(\frac{\pi \widehat{X}_2(\mathbf{X})}{7.5}\right)\sin(2\pi t), \\
\varphi_2(\mathbf{X},t) &= \widehat{X}_2(\mathbf{X}) + \frac{3}{2}\sin\left(\frac{\pi \widehat{X}_1(\mathbf{X})}{10}\right)\sin\left(\frac{\pi \widehat{X}_2(\mathbf{X})}{7.5}\right)\sin(4\pi t). \\
\varphi_3(\mathbf{X},t) &= X_3,
\end{aligned}$$

where $\widehat{X}_1(\mathbf{X})$, and $\widehat{X}_2(\mathbf{X})$ are defined as

$$\begin{aligned}
\widehat{X}_1(\mathbf{X}) &= 20 X_1, \\
\widehat{X}_2(\mathbf{X}) &= \frac{15}{2}\left(\frac{\tanh\left(\gamma\left(2X_2 - 1\right)\right)}{\tanh\left(\gamma\right)} + 1\right).
\end{aligned}$$

The constant velocity field used is $u_1 = 1, u_2 = 0.5$, and $u_3 = 0$, and the timestep is set to 1×10^{-3}. Figure 6 shows the deformed mesh at time $t = 0.15$ and the x-component of the computed velocity. Its value is one (upto machine precision) in all the control volumes. The error in computed x-component velocity, y-component velocity, and pressure with mesh refinement are tabulated in columns 2-4 of table 4. All three errors are of order machine precision, and therefore, the method preserves a uniform freestream condition. Also shown in columns 5-7 of table 6 is the error without using the DGCL advanced determinant of the Jacobian in the unsteady term of the momentum equation. Instead, the determinant of jacobian matrix computed from the geometry is used. The error is of order 10^{-2} and appears to stagnate with mesh refinement.

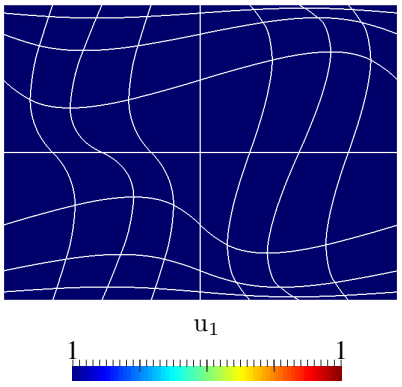

Figure 6: Freestream preservation test case at time $t = 0.15$.

Mesh	Error			Error without DGCL		
N	u_1	u_2	p	u_1	u_2	p
8	3.3e−14	1.6e−14	0	4.4e−2	7.3e−3	6.7e−2
16	3.9e−14	2.0e−14	0	4.4e−2	9.5e−2	1.3e−1
32	5.0e−14	2.5e−14	0	4.7e−2	1.2e−2	5.3e−2
64	4.4e−14	2.2e−14	0	4.7e−2	1.1e−2	1.4e−2

Table 4: History of convergence for the freestream preservation problem.

Turbulent channel with a deforming bottom wall

In this test case, we demonstrate the method's ability to handle large mesh deformation in a wall-bounded turbulent flow. A turbulent channel flow with a prescribed bottom wall motion is simulated at a friction Reynolds number of 180. The channel dimension is $2\pi \times 2 \times \pi$. The mesh motion is prescribed to be

$$\begin{aligned}\varphi_1(\mathbf{X},t) =& 2\pi X_1,\\ \varphi_2(\mathbf{X},t) =& \frac{1}{2}\left(2-\eta(X_1,X_3,t)\right)\frac{\tanh(\gamma(2X_2-1))}{\tanh(\gamma)}\\ &+\frac{1}{2}\left(2+\eta(X_1,X_3,t)\right)\\ \varphi_3(\mathbf{X},t) =& \pi X_3.\end{aligned} \tag{16}$$

where the bottom wall deformation $\eta(X_1, X_3, t)$ is prescribed as

$$\eta(X_1,X_3,t) = \alpha \sin(4\pi X_1)\sin(2\pi X_3)\sin(2\pi t/T_g),$$

and the reference domain is chosen to be the unit cube. Here, α, T_g, and γ are set to 0.6, 4, and 2.07, respectively. In the streamwise, wall-normal and spanwise directions, 341, 128, and 207 elements are respectively used. The mesh spacing is uniform in the streamwise and spanwise directions, and is non-uniform with a hyperbolic tangent stretching function in the wall-normal direction. Figure 7a shows an instantaneous contour of the streamwise velocity. The recirculation created by the downward moving bottom wall generates regions of large negative velocity in the troughs. Figure 7b shows the corresponding mesh.

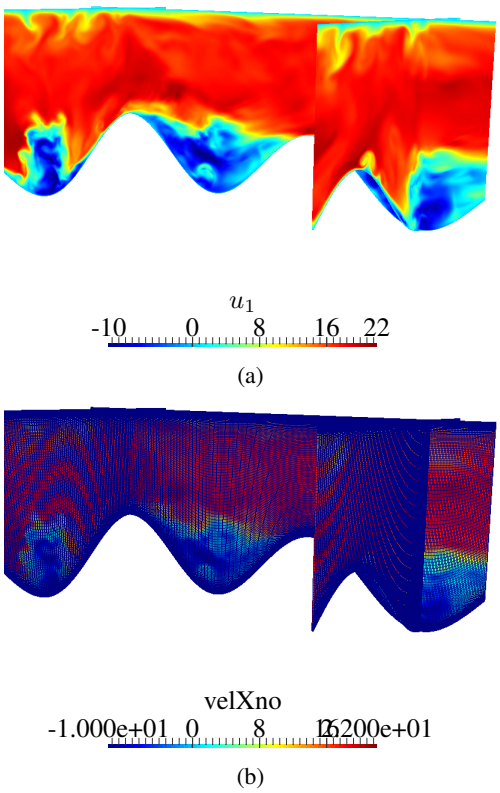

Figure 7: (a) Instantaneous contour of the streamwise component of velocity in the turbulent channel. (b) Instantaneous mesh of the turbulent channel

VISCOELASTIC IMPLEMENTATION IN MPCUGLES-SOLID

The dynamic equations for a linear incompressible viscoelastic solid are:

$$\begin{aligned}\rho^s \frac{\partial^2 u_i}{\partial t^2} &= \frac{\partial \sigma_{ij}}{\partial x_j} + l_i,\\ \frac{\partial u_k}{\partial x_k} &= 0,\end{aligned}$$

where u_i is the solid displacement, ρ^s is the solid density, and σ_{ij} is the stress given by $\sigma_{ij} = \tau_{ij} - p\delta_{ij}$, where p is the solid pressure, and τ_{ij} is the viscoelastic stress modeled using a Prony series as (Zienkiewicz and Taylor, 2005).

$$\begin{aligned}\tau_{ij}\left(\mathbf{x},\mathrm{t}\right) = 2\bar{\mu}\Big(&\mu_o \epsilon_{ij}\left(\mathbf{u}(\mathbf{x},t)\right) +\\ &\sum_{k=1}^{n}\mu_k \int_{-\infty}^{t} e^{-(t-\tau)/\lambda_k}\frac{\partial \epsilon_{ij}\left(\mathbf{u}\left(\mathbf{x},\tau\right)\right)}{\partial \tau}\,\mathrm{d}\tau\Big).\end{aligned} \tag{17}$$

Here, $\bar{\mu}$ is the zero-time shear modulus which relates to the zero-time Young's modulus and the Poisson's ratio (which is equal to 0.5) through the relation, $\bar{\mu} = \bar{E}/(2(1+\nu))$. $\{\lambda_k\}_{k=1}^{n}$ are the relaxation times, and $\{\mu_k\}_{k=0}^{\infty}$ are the dimensionless viscoelastic parameters that satisfy the

relations,

$$\sum_{k=0}^{n} \mu_k = 1, \text{ and } \mu_k \geq 0.$$

Extension of the below implementation to other viscoelastic stress models is straightforward.

The above equations are spatially discretized using the mixed finite element method (Hughes et al., 2000). The displacements and pressure are approximated using the continuous piecewise quadratic Lagrange local polynomials, and discontinuous linear global polynomials, respectively. We note that the approximation of pressure with global polynomials is crucial; local polynomials can reduce the accuracy (Arnold et al., 2001). The displacement unknowns are stored at the nodes, while the pressure unknowns are stored at points within the element. This discretization yields the below saddle-point matrix problem for the new timestep displacement d^{n+1} and pressure p^{n+1}.

$$\begin{aligned}
&\left[\frac{4}{\Delta t^2}\mathrm{M} + \left(\mu_0 + \sum_{k=1}^{n} \mu_k \Delta q_k\right)\overline{\mathrm{K}}\right]\mathrm{d}^{n+1} + \mathrm{G}\mathrm{p}^{n+1} = \\
&\mathrm{f}^{n+1} + \mathrm{M}\left[\frac{4}{\Delta t^2}\mathrm{d}^{n} + \frac{4}{\Delta t}\mathrm{v}^{n} + \mathrm{a}^{n}\right] \\
&\quad + \sum_{k=1}^{n}\left(-e^{-\Delta t/\lambda_k}\mathrm{q}_k^{n} + \Delta q_k \overline{\mathrm{K}}\mathrm{d}^{n}\right), \\
&\mathrm{G}^{\mathrm{T}}\mathrm{d}^{n+1} = \mathrm{g}^{n+1},
\end{aligned} \tag{18}$$

where M is the mass matrix, $\overline{\mathrm{K}}$ is the stiffness matrix constructed with the zero-time shear modulus $\overline{\mu}$, G and G^{T} are the gradient and divergence matrices, respectively, Δq_k is a viscoelastic parameter given by $\lambda_k/(\Delta t)\left(1 - e^{-\Delta t/\lambda_k}\right)$, where Δt is the timestep, f^{n+1} is the force vector, g^{n+1} is the contribution to divergence from the boundary conditions, and a^{n} is the previous timestep acceleration. The new timestep velocity, acceleration and viscoelastic stresses are updated as

$$\begin{aligned}
\mathrm{v}^{n+1} &= \frac{2}{\Delta t}\left(\mathrm{d}^{n+1} - \mathrm{d}^{n}\right) - \mathrm{v}^{n}, \\
\mathrm{a}^{n+1} &= \frac{4}{\Delta t^2}\left(\mathrm{d}^{n+1} - \mathrm{d}^{n}\right) - \frac{4}{\Delta t}\mathrm{v}^{n} - \mathrm{a}^{n}, \text{ and} \\
\mathrm{q}_k^{n+1} &= e^{-\Delta t/\lambda_k}\mathrm{q}_k^{n} + \Delta q_k \overline{\mathrm{K}}(\mathrm{d}^{n+1} - \mathrm{d}^{n}).
\end{aligned}$$

For a large scale solution of the above system of equations, a good parallel preconditioner is crucial, especially for soft materials. It turns out that black-box preconditioners provided by the Trilinos Ifpack2 package are not effective for parallel solution. For e.g., using the incomplete LU factorization on four processors increases the number of GMRES iterations by a factor of 10 compared to that on a single processor. Therefore, we implemented the Silvester-Kay-Wathen preconditioner (Silvester et al., 2001) given by

$$\mathrm{P} = \begin{bmatrix} \mathrm{K}_{\text{eff}} & \mathrm{G} \\ 0 & \left(\overline{\mu}\Delta t \mathrm{M}_p^{-1} + \frac{1}{\Delta t}\left[\frac{1}{h_1 h_2 h_3}\mathrm{G}^{\mathrm{T}}\mathrm{G}\right]^{-1}\right)^{-1} \end{bmatrix}.$$

Here, $\mathrm{K}_{\text{eff}} = \left[\frac{4}{\Delta t^2}\mathrm{M} + \left(\overline{\mu}_0 + \sum_{k=1}^{n}\mu_k \Delta q_k\right)\overline{\mathrm{K}}\right]$, M_p is the mass matrix constructed using the pressure basis functions, h_1, h_2, and h_3 are the characteristic mesh sizes along each dimension. This preconditioner along with our in-house implementation of flexible GMRES was found to be the most effective choice.

Validation

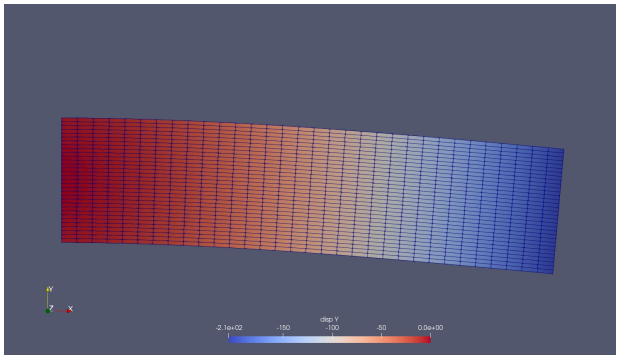

(a)

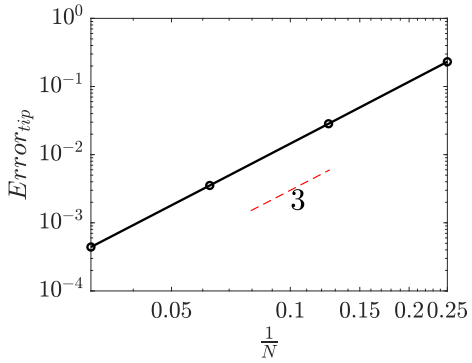

(b)

Figure 8: a) Incompressible cantilever beam deformation. b) Tip deflection's absolute error with mesh refinement. N is the number of element along each direction.

Static, dynamic, and eigenvalue problems are solved to validate the implementation. Figure 8a shows the static deformation of a cantilever beam under plain strain. Figure 8b shows the error in tip deflection with mesh refinement. The tip displacements converge with the expected third-order accuracy. This problem validates the two-dimensional stiffness and gradient matrices.

The three-dimensional stiffness, gradient and mass matrices are validated by computing a few smallest eigenvalues of an incompressible clamped elastic square plate using three-dimensional solid elements. The incompressible eigenvalue problem is

$$\begin{bmatrix} \mathrm{K} & \mathrm{G} \\ \mathrm{G}^{\mathrm{T}} & 0 \end{bmatrix}\begin{bmatrix} \mathrm{v}_{\mathrm{j}}^{\mathrm{d}} \\ \mathrm{v}_{\mathrm{j}}^{\mathrm{p}} \end{bmatrix} = \omega_{\mathrm{j}}{}^2 \begin{bmatrix} \mathrm{M} & 0 \\ 0 & 0 \end{bmatrix}\begin{bmatrix} \mathrm{v}_{\mathrm{j}}^{\mathrm{d}} \\ \mathrm{v}_{\mathrm{j}}^{\mathrm{p}} \end{bmatrix}.$$

Here, ω_{j} are the natural frequencies, $\mathrm{v}_{\mathrm{j}}^{\mathrm{u}}$ is the natural modes' displacement degrees of freedom and $\mathrm{v}_{\mathrm{j}}^{\mathrm{p}}$ is the natural modes' pressure degrees of freedom. The above eigenvalue problem is an indefinite generalized eigenvalue problem. Therefore, the above problem is first converted to a standard eigenvalue problem by premultiplying with the inverse of the left-hand side matrix. The resulting eigenvalue problem is then solved using the Block Krylov Schur algorithm available in Trilinos Anasazi package (Trilinos Project Team). Table 5 shows the first two natural frequencies and the reference values for comparison. The computed results agree well with the reference results.

Mode	Computed	Reference (Leissa, 1969)
1	36.17	36
2	73.67	73.41

Table 5: Natural frequencies ($\omega_j \sqrt{\frac{\rho h}{D}} L^2$) of a clamped incompressible elastic square plate.

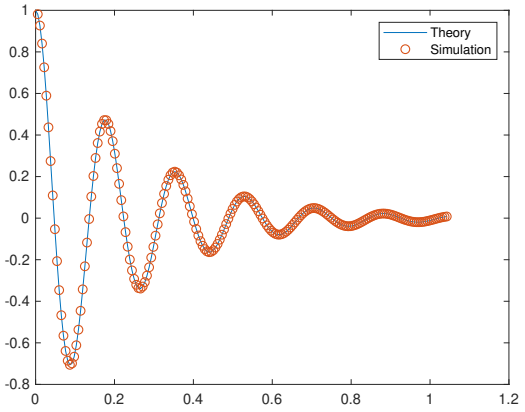

Figure 9

The time integration and the inelastic stress contribution are validated by simulating the free vibration of a clamped viscoelastic square plate. The displacement is initialized to the first mode shape of the plate. The initial velocity is set to zero. A single term Prony series is assumed. The viscoelastic parameters μ_0, μ_1, and λ_1 are set to 0.15, 0.85, and 0.1, respectively. For the prescribed initial condition, the response will only be along the first mode, i.e., $\mathrm{d}(t) = d_1(t)\mathrm{v}_1^{\mathrm{d}}$, where $d_1(t)$ is the component, and $\mathrm{v}_1^{\mathrm{d}}$ is the first mode. Figure 9 compares $d_1(t)$ computed from the numerical solution to the analytical solution. The numerical solution agrees with the analytical solution.

TWO-WAY COUPLING

Problem

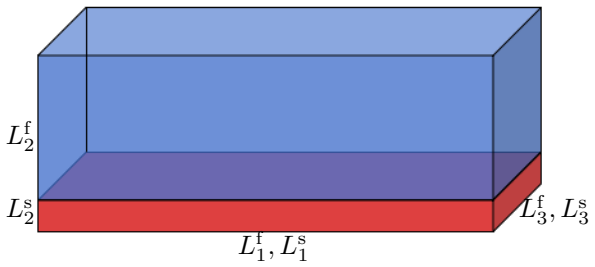

Figure 10: Schematic of the problem in the undeformed configuration.

Figure 10 shows the schematic of the considered two-way coupled FSI problem in the undeformed configuration, i.e., at time $t = 0$. The blue and red boxes denote the fluid and solid domains, respectively. The fluid domain is a channel, and the solid domain is a compliant wall situated at the bottom of the channel. The dimension of the fluid and solid domains are $L_1^{\mathrm{f}} \times L_2^{\mathrm{f}} \times L_3^{\mathrm{f}}$ and $L_1^{\mathrm{s}} \times L_2^{\mathrm{s}} \times L_3^{\mathrm{s}}$, respectively. The fluid within the channel is assumed to be incompressible, and the compliant wall is assumed to be composed of an incompressible viscoelastic material, for e.g., polydimethylsiloxane.

Governing equations

The governing equations in the fluid domain are the incompressible Navier-Stokes equations solved in the ALE frame of reference.

$$\begin{aligned} &\left.\frac{\partial \mathbf{u}_{\mathrm{f}}(\boldsymbol{\varphi}_{\mathrm{f}}(\mathbf{X},t),t)}{\partial t}\right|_{\left(\boldsymbol{\varphi}_{\mathrm{f}}^{-1}(\mathbf{x},t),t\right)} - \mathbf{v}_{\mathrm{g}} \cdot \boldsymbol{\nabla}\mathbf{u}_{\mathrm{f}} + \boldsymbol{\nabla} \cdot \left(\mathbf{u}_{\mathrm{f}}\mathbf{u}_{\mathrm{f}}^{\mathrm{T}}\right) = \\ &-\boldsymbol{\nabla} p_{\mathrm{f}} + \frac{1}{Re}\boldsymbol{\nabla}^2 \mathbf{u}_{\mathrm{f}} + \boldsymbol{\ell}_{\mathrm{f}} \text{ in } \Omega_{\mathrm{f}}(t), \text{ and} \\ &\boldsymbol{\nabla} \cdot \mathbf{u}_{\mathrm{f}} = 0 \text{ in } \Omega_{\mathrm{f}}(t). \end{aligned} \tag{19}$$

Here, $\mathbf{u}_{\mathrm{f}}$ and p_{f} are the fluid velocity and pressure, respectively, $\Omega_{\mathrm{f}}(t)$ is the current fluid domain at time t, $\boldsymbol{\ell}_{\mathrm{f}}$ is the body force, $\boldsymbol{\varphi}_{\mathrm{f}}(\mathbf{X},t)$ is the ALE mapping, and $\mathbf{v}_{\mathrm{g}} = \partial\boldsymbol{\varphi}_{\mathrm{f}}(\mathbf{X},t)/\partial t$ is the grid velocity. $Re = \rho_{\mathrm{f}} U_{\mathrm{f}} L_{\mathrm{f}}/\mu_{\mathrm{f}}$ is the Reynolds number, where ρ_{f}, U_{f}, and L_{f} are the reference fluid density, velocity, length scale, respectively, and μ_{f} is the dynamic viscosity. In the solid domain, we solve a modified form of the dynamic linear incompressible elasticity equations in the Lagrangian frame of reference. The modification enforces the incompressibility of the solid in the current domain instead of the reference domain, and accordingly modifies the contribution of pressure to the total stress. It is important to note that

without these modifications, the coupled problem is not solvable. The modified solid equations are:

$$\frac{\rho_\mathrm{s}}{\rho_\mathrm{f}}\frac{\partial^2 \mathbf{d}_\mathrm{s}}{\partial t^2} = -\boldsymbol{\nabla}_{\mathbf{X}}\cdot\left(P_\mathrm{s}J_\mathrm{s}\mathbf{F}_\mathrm{s}^{-T}\right) + \boldsymbol{\nabla}_{\mathbf{X}}\cdot\boldsymbol{\mathcal{T}}_\mathrm{s} + \mathbf{L}_\mathrm{s} \text{ in } \Omega_\mathrm{s}^0, \text{ and}$$
$$\boldsymbol{\nabla}_{\mathbf{X}}\cdot\left(J_\mathrm{s}\mathbf{F}_\mathrm{s}^{-1}\mathbf{U}_\mathrm{s}\right) = 0 \text{ in } \Omega_\mathrm{s}^0. \tag{20}$$

where $\boldsymbol{\mathcal{T}}_\mathrm{s}$ is defined by a linear viscoelastic relation (equation 17). In addition, the sum of the mass flux integral at the fluid and solid Dirichlet boundaries should be equal to zero. This ensures that the coupled problem is solvable. For uniqueness of the fluid and solid pressures, we require that the integral of pressure in the combined fluid-solid domain should be zero.

The conditions that couple the fluid and solid solutions are: i) Geometric adherence condition on the fluid ALE mapping and the solid displacement. ii) Continuity of velocity at the fluid-solid interface. iii) Continuity of the normal component of stress at the fluid-solid interface. iv) A condition on the fluid and solid pressure averages. v) A condition on the flux of the common fluid-solid interface velocity. The equation below describes these conditions.

$$\begin{aligned}
&\text{(i)}\ \boldsymbol{\varphi}_\mathrm{f}(\mathbf{X},t) = \mathbf{X} + \mathbf{d}_\mathrm{s}(\mathbf{X},t),\\
&\text{(ii)}\ \mathbf{u}_{\Gamma\mathrm{f}}(\boldsymbol{\varphi}_\mathrm{f}(\mathbf{X},t),t) = \mathbf{U}_{\Gamma\mathrm{s}}(\mathbf{X},t),\\
&\text{(iii)}\ \boldsymbol{\sigma}_\mathrm{f}(\boldsymbol{\varphi}_\mathrm{f}(\mathbf{X},t),t)J_\mathrm{f}(\mathbf{X},t)\mathbf{F}_\mathrm{f}^{-T}(\mathbf{X},t)\mathbf{N}_\mathrm{f}(\mathbf{X}) +\\
&\qquad \mathbf{P}_\mathrm{s}(\mathbf{X},t)\mathbf{N}_\mathrm{s}(\mathbf{X}) = 0,\\
&\text{(iv)}\ \overline{p}_\mathrm{f}(t)|\Omega_\mathrm{f}(t)| + \overline{p}_\mathrm{s}(t)|\Omega_\mathrm{s}(t)| = 0,\\
&\text{(v)}\ \int_{\Gamma_\mathrm{fs}(t)} \mathbf{u}_{\Gamma\mathrm{f}}\cdot\mathbf{n}_\mathrm{f}\,\mathrm{d}\Gamma = 0.
\end{aligned} \tag{21}$$

Here, $\mathbf{X}$ is a point on the undeformed fluid-solid interface Γ_fs^0. $\boldsymbol{\sigma}_\mathrm{f}(\mathbf{x},t)$ is the fluid Cauchy stress tensor. $\mathbf{F}_\mathrm{f}$ is $\boldsymbol{\nabla}_{\mathbf{x}}\boldsymbol{\varphi}_\mathrm{f}$, and J_f is $\det(\mathbf{F}_\mathrm{f})$. $\mathbf{N}_\mathrm{f}$ and $\mathbf{N}_\mathrm{s}$ are unit normals to Γ_fs^0 pointing outward to the fluid and solid domain, respectively. $|\Omega_f(t)|$ and $|\Omega_s(t)$ are the time-dependent volumes of the fluid and solid domain, respectively.

Two-way coupled simulation with sequential fixed point iteration

Below, we present some preliminary results of the two-way coupled problem using a modified sequential fixed-point coupling algorithm. Some details of this algorithm are given below. The boundary conditions of the fluid subproblem are: Periodic boundary condition along the streamwise and spanwise directions. Dirichlet velocity boundary condition on the top and bottom wall. The top wall is stationary. The Dirichlet data for the bottom wall is supplied by the coupling algorithm. The boundary conditions of the solid subproblem are: all sides except the fluid-solid interface are clamped. Stress boundary condition is used on the fluid-solid interface and the coupling algorithm provides the stress data. The coupling algorithm is as follows. At each timestep, the fluid and solid solutions are coupled via the fixed-point interface problem below:

$$\begin{aligned}
&\text{Find } \mathbf{d}_\Gamma^{n+1},\ \overline{p}_\mathrm{f}^{n+1},\ \text{such that}\\
&\mathbf{d}_\Gamma^{n+1} = \mathbf{S}_{N\to D}^{n+1}(\mathbf{F}_{D\to N}^{n+1}(\mathbf{d}_\Gamma^{n+1},\overline{p}_\mathrm{f}^{n+1}))\\
&\overline{p}_\mathrm{f}^{n+1}|\Omega_\mathrm{f}^{n+1}| + \overline{p}_\mathrm{s}^{n+1}|\Omega_\mathrm{s}^{n+1}| = 0.
\end{aligned} \tag{22}$$

Here, $\mathbf{d}_\Gamma^{n+1}$ is the fluid-solid interface displacement at timestep $n+1$. $\mathbf{S}_{N\to D}^{n+1}$ denotes the solid subproblem at timestep $n+1$. The subscript $N\to D$ means that it takes the Neumann data (normal-component of stresses) as the input at the fluid-solid interface boundary and returns the Dirichlet data (displacement) on the same boundary as the output. Similarly, $\mathbf{F}_{D\to N}^{n+1}$ denotes the fluid subproblem at timestep $n+1$. The subscript $D\to N$ means that it takes the Dirichlet data (displacement/velocity) as input at the fluid-solid interface boundary and returns the Neumann data (normal-component of stresses) on the same boundary as the output. In the usual version of the sequential fixed-point iteration (Mehl et al., 2016), the average fluid-pressure is not an unknown in the interface problem. Having it as an unknown is essential here because the fluid pressure is determinable only up to an additive constant (since we use only periodic and Dirichlet boundary conditions for the fluid subproblem). Arbitrarily setting this average (to say zero) would arbitrarily change the average pressure load on the compliant wall which can deform it aphysically. The iterative algorithm to find the solution to the interface problem is:

$$\begin{aligned}
&\text{For } k = 0,\ldots\\
&\mathbf{d}_\Gamma^{k+1} = \mathbf{d}_\Gamma^{k} + \omega^k(S_{N\to D}^{n+1}(F_{D\to N}^{n+1}(\mathbf{d}_\Gamma^{k+1},\overline{p}_\mathrm{f}^{k})) - \mathbf{d}^k)\\
&\overline{p}_\mathrm{f}^{k+1}|\Omega_\mathrm{f}^{*}| + \overline{p}_\mathrm{s}^{k}|\Omega_\mathrm{s}^{*}| = 0\\
&\text{If } \|\mathbf{d}_\Gamma^{k+1} - \mathbf{d}_\Gamma^{k}\|_2 \le \epsilon, \text{ then exit for loop}
\end{aligned} \tag{23}$$

Here, Ω_f^* and Ω_s^* are the predicted fluid and solid domain at timestep $n+1$, respectively. ω^k is the dynamic relaxation factor. It is determined using the Aitken's method (Küttler and Wall, 2008). The fluid ($F_{D\to N}^{n+1}$) and solid subproblems ($S_{N\to D}^{n+1}$) are solved using MPCUGLES and MPCUGLES-SOLID, respectively. Here, ϵ is the convergence tolerance of the interface displacement.

The parameters of the problem are as follows. The friction Reynolds number is 180. The dimensions of the fluid domain are $L_1^f = 2\pi\delta$, $L_2^f = 2\delta$, and $L_3^f = \pi\delta$. For the solid domain, the dimensions are $L_1^s = 2\pi\delta$, $L_2^s = 0.1\delta$, and $L_3^s = \pi\delta$. For the compliant wall, the density, Young's modulus, and Poisson's ratio are set to $100\rho^f$, $10^5\rho^f {u_\tau^f}^2$, and 0.5, respectively. Along the streamwise and spanwise direction, 120 and 82 uniform elements are used, respectively, for both the fluid and solid. In the wall-normal direction, 82 elements with hyperbolic tangent stretching are used in the fluid and 5 uniform elements are used in the solid. The resulting streamwise

grid resolution is $\Delta x_1^{+f} = \Delta x_1^{+s} = 9.42$. The spanwise resolution is $\Delta x_3^{+f} = \Delta x_3^{+s} = 6.9$. The wall-normal resolution in the fluid is $\Delta y_w^{+f} = 0.56$. The timestep is chosen to be $10^{-5}\delta/u_\tau^f$. A total of 144 processors are used. Both the fluid and the solid subproblems are partitioned into 144 processors. Note that the fluid and solid meshes match at the fluid-solid interface. This simplifies the transfer of the fluid loads to the solid and the transfer of the solid displacements to the fluid. The fluid problem is first run with a rigid bottom wall until it reaches a statistically stationary state. The two-way coupling is then turned on and the coupled problem is solved.

Figure 11 shows an instantaneous visualization of the two-way coupled problem. On the compliant wall, away from the clamped boundaries, we observe streaky deformation. The maximum wall-normal displacement and velocity are of the order $10^{-3}\delta_\nu$ and $10^{-3}u_\tau^f$, respectively. Even though the deformation is small, it affects the flow discharge. This might indicate that the deformation has a non-negligible impact on the fluid flow.

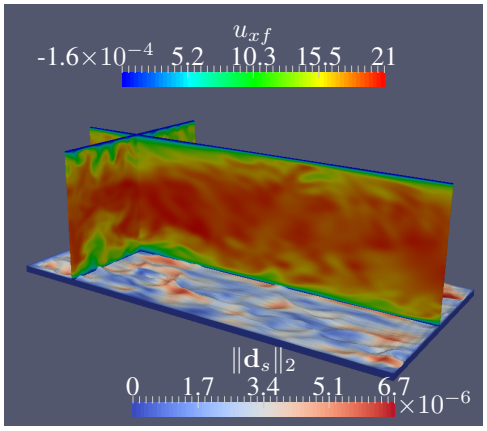

Figure 11: Instantaneous visualization. Velocity and displacement are normalized with u_τ^f and δ, respectively. The solid displacements are amplified by a factor of 2×10^4.

supplied by the coupling algorithm.

Fluid executable	Solid executable
$\frac{J_f^{n+1}-J_f^n}{\Delta t} = \frac{3}{2}\mathrm{GRHS}_f^n - \frac{1}{2}\mathrm{GRHS}_f^{n-1}$	
$\frac{\hat{U}_f J_f^{n+1} - U_f^n J_f^n}{\Delta t} =$ $\frac{3}{2}\left(-\mathrm{NL}_f^n + \frac{1}{Re}\mathrm{VISC}_f^n + \mathrm{BF}_f^n\right) -$ $\frac{1}{2}\left(-\mathrm{NL}_f^{n-1} + \frac{1}{Re}\mathrm{VISC}_f^{n-1} + \mathrm{BF}_f^{n-1}\right)$	
Extrapolate d_Γ^* Compute ALE mapping $\varphi_f^*(d_\Gamma^*)$	Extrapolate $\Omega_{s,h}^*$ Recompute G_s^*, and ${G_s^*}^T$

Recompute M_Γ^*, and g_Γ^*
Construct initial guess $u_\Gamma^{n+1,0}$ s.t. ${g^*}^T u_\Gamma^{n+1,0} = s_\Gamma^{n+1}$
Compute initial residual, $r_\Gamma^{n+1,0}$= FSICouplingKernel $(u_\Gamma^{n+1,0})$
k=0; win=$u_\Gamma^{n+1,0}$
do while (.true.)
(isnc,isc,wout)= matFreeGMRESKernel (k,win,tol,maxIter)
if(isnc) stop "GMRES did not converge."
if(.not. isc) win= FSICouplingKernel $(u_\Gamma^{n+1,0}$+wout)-$r_\Gamma^{n+1,0}$
if(isc) then
$u_\Gamma^{n+1} = u_\Gamma^{n+1,0}$+wout,
compute the fluid and solid solution by solving
r_Γ^{n+1}= FSICouplingKernel (u_Γ^{n+1}), and
verify r_Γ^{n+1} to be small
endif
k=k+1
enddo	

$U_f^{n+1} = \hat{U}_f - \Delta t G^* P_f^{n+1}$	$d_s^{n+1} = d_s^n + \frac{\Delta t}{2}\left(U_s^{n+1} + U_s^n\right)$ $a_s^{n+1} = \frac{2}{\Delta t}\left(U_s^{n+1} - U_s^n\right) - a_s^n$

Table 6: Two-way coupling algorithm.

r_Γ= FSICouplingKernel (v_Γ)

Fluid executable	Solid executable
Input: v_Γ	
$-L^* P_f^{n+1} = b(v_\Gamma)$, and require $(\sum_{cv_s} p_{f,icv}^{n+1}\lvert\Omega_{f,icv}^*\rvert)/\lvert\Omega_f^*\rvert = 0.$ Post-process fluid solution to form $F_{f\Gamma}$ Compute $H_{f\Gamma}^{n+1} = [M_\Gamma^*]^{-1} F_{f\Gamma}$	$C_{s,\mathrm{eff}} U_s^{n+1} + G_s^* P_s^{n+1} = b_u^{n+1}(v_\Gamma)$ ${G_s^*}^T U_s^{n+1} = b_p^{n+1}(v_\Gamma)$, and require $(\int_{\Omega_f^*} p_s^{n+1}\,d\Omega)/\lvert\Omega_s^*\rvert = 0.$ Post-process solid solution to form $F_{s\Gamma}$ Compute $H_{s\Gamma}^{n+1} = [M_\Gamma^*]^{-1} F_{s\Gamma}$
Set $\lambda(v_\Gamma)$ to $\frac{-g_\Gamma^{*T}\left[H_{f\Gamma}^{n+1} - H_{s\Gamma}^{n+1}\right]}{g_\Gamma^{*T}[M_\Gamma^*]^{-1} g}$	
Set r_Γ to $H_{f\Gamma}^{n+1} - H_{s\Gamma}^{n+1} + \lambda(v_\Gamma)[M_\Gamma^*]^{-1} g_\Gamma^*$	
Output: r_Γ	

Table 7: The FSI coupling kernel.

The proposed method

Notice that in the sequential fixed-point coupling algorithm, the fluid and solid solvers have to be executed one after the other. The proposed method allows for simultaneous execution of the two solvers. The boundary conditions for the fluid subproblem remains the same as that in the fixed-point coupling algorithm. However, the boundary conditions of the solid subproblem are different. They are: Dirichlet boundary conditions are used on all sides. The left, right, and bottom sides are clamped by setting the Dirichlet data to zero. On the fluid-solid interface boundary (the top side), the Dirichlet data is

A brief description of the proposed method is as follows. The predictor equations of the fluid are first advanced using the explicit Adams-Bashforth scheme. The new timestep displacement of the fluid-solid is extrapolated from the previous timesteps, and the corresponding ALE mapping in the fluid is computed via the Laplacian extension approach (Nobile, 2001). The solid domain is also extrapolated from the previous timesteps, and the new timestep gradient and divergence matrices are computed. At each timestep, the fluid and solid solution are coupled by solving the below discrete

problem at the interface:

$$\begin{aligned}&\text{Find } \mathrm{u}_\Gamma^{n+1},\ \overline{p}_\mathrm{f}^{n+1},\ \text{and } \overline{p}_\mathrm{s}^{n+1},\ \text{such that}\\&\|\mathrm{H}_{\mathrm{f}\Gamma}^{n+1}(\mathrm{u}_\Gamma^{n+1},\overline{p}_\mathrm{f}^{n+1}) - \mathrm{H}_{\mathrm{s}\Gamma}^{n+1}(\mathrm{u}_\Gamma^{n+1},\overline{p}_\mathrm{s}^{n+1})\|_{\ell^2} \text{ is minimum,}\\&{\mathrm{g}_\Gamma^*}^T\,\mathrm{u}_\Gamma^{n+1} = s_\Gamma^{n+1},\ \text{and}\\&\overline{p}_\mathrm{f}^{n+1}|\Omega_\mathrm{f}^*| + \overline{p}_\mathrm{s}^{n+1}|\Omega_\mathrm{s}^*| = 0.\end{aligned} \tag{24}$$

Here, u_Γ^{n+1} is the new timestep velocity at the nodes of the interface mesh. $\overline{p}_\mathrm{f}^{n+1}$, and $\overline{p}_\mathrm{s}^{n+1}$, are the new timestep fluid and solid average pressure, respectively. $\mathrm{H}_{\mathrm{f}\Gamma}^{n+1}$ and $\mathrm{H}_{\mathrm{s}\Gamma}^{n+1}$ are the discrete fluid and solid Steklov-Poincare operators, respectively. $|\Omega_\mathrm{f}^*|$ and $|\Omega_\mathrm{s}^*|$ are the volumes of the discrete fluid and solid domains, respectively. g^* is the discrete gradient at the interface, and s_Γ^{n+1} is the contribution from the fixed nodes at the interface. To solve the above interface problem, we developed a novel solution procedure using the matrix-free implementation of GMRES. Note that the fluid and solid equations are solved using MPCUGLES and MPCUGLES-SOLID, respectively.

Algorithm in table 6 summarizes the method and also its multiple-program multiple-data implementation. The two main kernels of the algorithm are the FSI coupling kernel (denoted as 'FSICouplingKernel'), and the matrix-free GMRES kernel (denoted as 'matFreeGMRESKernel'). The FSI coupling kernel shown in algorithm 7 yields the residual vector r_Γ given a GMRES Arnoldi vector v_Γ. Within this kernel, we solve the pressure Poisson equation within the fluid, and the saddle point problem within the solid. The matrix-free GMRES kernel performs the operations of the GMRES algorithm which includes i) orthogonalizing the matrix-vector products, ii) building the upper Hessenberg matrix, iii) checking whether the residual is smaller than the specified tolerance (denoted as 'tol'), iv) checking whether the number of GMRES iterations has reached the specified maximum number (denoted as 'maxIter'), and v) solving the projected least squares problem when the iterations converge. To compute the matrix-vector products required at each iteration 'k', the kernel uses reverse communication through the work vectors 'wout' and 'win'.

Some details of the multiple program, multiple data implementation are discussed. The fluid and solid executables are started simultaneously as `mpiexec -n np_f ./fsolver_exe : -n np_s ./ssolver_exe`. This command runs the fluid solver executable, `fsolver_exe`, in the first `0` to `np_f`-1 ranks, and the solid solver executable, `ssolver_exe`, in the remaining `np_f` to `np_f`+`np_s`-1 ranks. In tables 6 and 7, the cells shaded in blue and red show the tasks performed by the fluid and solid executable, respectively. To perform the unshaded tasks, the two executables need to be synchronized. The fluid and solid solver tasks between any two consecutive synchronization points can be performed in parallel. Therefore, ours is a parallel coupling approach. To exchange data between the processors running the fluid and solid executables, we use the global MPI communicator, `MPI_COMM_WORLD`. For communication within the fluid processors and within the solid processors, we use a sub-communicator created via `MPI_COMM_SPLIT`.

Validation of the proposed method

The method of manufactured solution is used for validation. The undeformed fluid and solid domains are assumed to be two unit cubes. The exact fluid velocities and pressure are assumed to be

$$\begin{aligned}u_{\mathrm{f},1}(x_1,x_2,x_3,t) &= 0\\u_{\mathrm{f},2}(x_1,x_2,x_3,t) &= \alpha\sin(k_1x_1)\omega\sin(2\omega t)\\u_{\mathrm{f},3}(x_1,x_2,x_3,t) &= 0\\p_\mathrm{f}(x_1,x_2,x_3,t) &= \alpha\sin(k_1x_1)\sin(\omega t).\end{aligned}$$

The constants k_1 and ω are both set to 2π, and the constant α is set to 0.1. The exact solid displacement and pressure are taken to be

$$\begin{aligned}d_{\mathrm{s},1}(X_1,X_2,X_3,t) &= 0,\\d_{\mathrm{s},2}(X_1,X_2,X_3,t) &= \alpha\sin(k_1X_1)\sin^2(\omega t)\\d_{\mathrm{s},3}(X_1,X_2,X_3,t) &= 0\\p_\mathrm{s}(x_1,x_2,x_3,t) &= \alpha\sin(k_1x_1)\sin(\omega t).\end{aligned}$$

The above fluid and solid velocities correspond to an incompressible generalized shear deformation. Using the above solution, the FSI problem data, i.e., the body force within the fluid and solid, the fluid and solid Dirichlet boundary data on the boundary surfaces except the fluid-solid interface, the fluid and solid initial conditions, and the jump in their stresses at the fluid-solid interface, are set. Note that the Dirichlet boundary data for this test case is different compared to the two-way coupled channel case. The solid is assumed to an incompressible elastic material, i.e., μ_0 is set to one and $n_{\text{inelastic}}$ is set to zero. The non-dimensional zero-time Young's modulus, and Poisson's ratio are set to 3, and 0.5, respectively. The non-dimensional density of 1 is used to test the robustness of our method in the presence of added-mass effect. The Reynolds number of the fluid is set to 100.

Both fluid and solid meshes use 32 elements along X_1 direction, 5 elements along X_2 direction, and 5 elements along X_3 direction. The test is conducted using 8 processors for the fluid solver, and 8 processors for the solid solver. Note that we have also successfully tested the implementation for number of fluid processors $\neq$ number of solid processors. The coupled problem is solved until $T = 1$ with a time step of 10^{-3}.

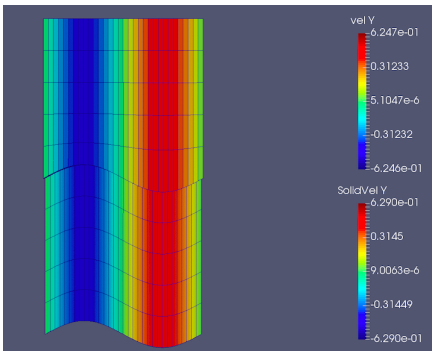

Figure 12: Instantaneous snapshot of the computed fluid and solid solutions.

Figure 12 shows an instantaneous snapshot of the computed fluid and solid solutions. The figure shows the contours of the X_2 component of the fluid and solid velocity. To verify our coupling approach and the correctness of our parallel implementation, we measure the error in the solid displacements e_{u_s} which is defined as follows.

$$e_{u_s} = \max_{1 \le n \le N} \|\mathbf{U}^n_{s,h}(\mathbf{X}) - \mathbf{U}(\mathbf{X}, t^n)\|_{L_2(\Omega^0_s)},$$

where N is the total number of timesteps. The computed error e_{u_s} is $\approx 5 \times 10^{-5}$. This verifies our coupling approach and the correctness of our parallel implementation. Simulations to check the parallel efficiency of the method and to verify the correctness for turbulent FSI problems are currently being conducted.

ONE-WAY COUPLED PLATE EXCITATION

Problem

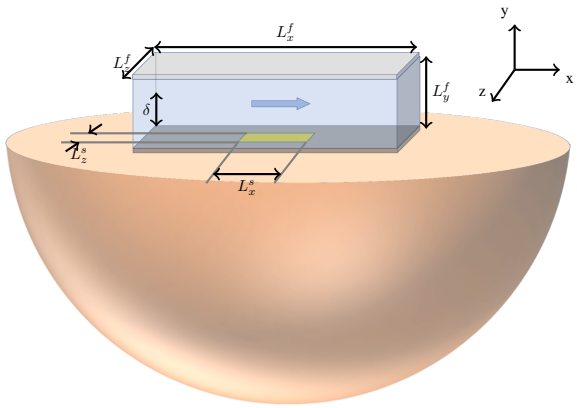

Figure 13: Computational domain.

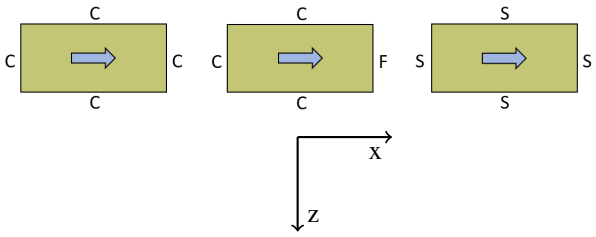

Figure 14: Plate boundary conditions. Arrow denotes the direction of mean flow.

Figure 13 shows the problem setup. The blue, yellow, and orange regions denote the fluid, solid, and acoustic subdomains, respectively. The fluid subdomain is a channel of size $L^f_x \times L^f_y \times L^f_z$, where $L^f_x = 6\pi\delta$, $L^f_y = 2\delta$, and $L^f_z = 2\pi\delta$. The solid subdomain is a plate of size $L^s_x \times L^s_y \times L^s_z$, where $L^s_x = (6\pi/5)\,\delta$, the plate thickness $L^s_y = 0.004\delta$, and $L^s_z = (2\pi/5)\,\delta$. The acoustic subdomain is the entire bottom half-space below the plate. The large streamwise (L^f_x) and spanwise (L^f_z) extents of the channel are essential to include the contribution of large-scale turbulent structures to the wall-pressure fluctuations.

The plate is centered and baffled. The three plate boundary conditions considered are – all four sides clamped (CCCC), three sides clamped and one side free (CCCF), and all four sides simply supported (SSSS). Figure 14 shows a schematic of the different boundary conditions and also the orientation of the edges. Two plate materials are considered: synthetic rubber – a soft material, and stainless steel – a stiff material. The two materials are assumed to be elastic. For synthetic rubber, the density, Young's modulus, and Poisson's ratio are set to $1522\text{kg}\,\text{m}^{-3}$, 50MPa, and 0.4, respectively. For stainless steel, the density, Young's modulus, and Poisson's ratio are set to $7500\text{kg}\,\text{m}^{-3}$, 180GPa, and 0.305, respectively. The fluid inside the channel is chosen to be incompressible air at room temperature. The channel half height, δ, is chosen to be 1.25cm. The friction Reynolds numbers considered are $Re_\tau = 180$ and $Re_\tau = 400$, where Re_τ is defined to be $u^f_\tau \delta/\nu^f$. To increase the Reynolds number, we increase the flow velocity while keeping the remaining parameters constant. This yields a friction velocity, u^f_τ, of around $0.225\text{m}\,\text{s}^{-1}$ for $Re_\tau = 180$ and around $0.5\text{m}\,\text{s}^{-1}$ for $Re_\tau = 400$. For structural damping, we use the Rayleigh damping model. The stiffness-proportional damping coefficient is set to zero and the mass-proportional damping coefficient is computed such that the loss factor is 0.05 at the first natural frequency of the plate. The acoustic medium is assumed to be air. Assuming room temperature, the speed of sound is then $343\text{m}\,\text{s}^{-1}$. In total, we have 12 cases – two Reynolds number, two plate materials, and three plate boundary conditions.

Simulation methodology

For both Reynolds numbers, the turbulent flow is first simulated by assuming the bottom wall to be rigid. Once the flow becomes statistically stationary, the wall-pressure fluctuations are stored for a total time of $30\delta/u_\tau^f$ for $Re_\tau = 180$, and $23\delta/u_\tau^f$ for $Re_\tau = 400$. The channel flow simulation is performed in a moving frame of reference for better accuracy (Bernardini et al., 2013). Therefore, the pressure fluctuations are converted to a stationary frame, and then used to compute the plate response for each Reynolds number, plate material and plate boundary condition. The far-field sound is computed from the plate response. We discard the initial $15\delta/u_\tau^f$ units of the simulated response and sound for $Re_\tau = 180$ cases, and $8\delta/u_\tau^f$ units for $Re_\tau = 400$ cases because it predominantly contains the plate's transient response. The remaining data is used to compute the statistics of the plate displacement and sound.

The DNS simulation of the turbulent channel flow is performed by solving the incompressible Navier-Stokes equations using MPCUGLES (Mahesh et al., 2004). Table 8 shows the DNS mesh resolution. The validation of the computed solution can be found in Anantharamu and Mahesh (2020). The plate response is simulated by solving the dynamic linear elasticity equations using MPCUGLES-SOLID. The plate is discretized with 27-node hexahedral finite elements. Table 9 shows the solid mesh resolution. Note that the fluid and solid meshes match at the fluid-solid interface, and therefore, transferring the pressure fluctuations from the fluid to the solid mesh is straightforward. For validation of MPCUGLES-SOLID for plate problems, we refer the reader to Anantharamu and Mahesh (2021). To compute the sound radiated by the vibrating plate, we solve the wave equation for acoustic pressure in the acoustic domain using a Green's function methodology. The plate acceleration supplies the Neumann boundary condition at the interface between the plate and the acoustic medium. The sound pressure is computed at discrete points on a polar grid in the acoustic domain, and at discrete time instants. These points are $(r_i\cos(\theta_j), r_i\sin(\theta_j), \pi)$, where

$$r_i = r_o + i\Delta r;\ \theta_j = \theta_o + j\Delta\theta;\ r_o = 10\pi;\ \theta_o = \pi;$$
$$\Delta r = \frac{160\pi}{N_r};\ \Delta\theta = \frac{\pi}{N_\theta};$$
$$i = 1, \ldots, N_r, \text{ and } j = 1, \ldots, N_\theta.$$

Here, N_r and N_θ are the number of points along radial and angular directions, respectively. N_r is set to 15, and N_θ is set to 19. The acoustic solver which is a module within MPCUGLES-SOLID has also been validated (not shown). All three solvers use a non-dimensional timestep of $\Delta t\, u_\tau^f/\delta = 5\times10^{-4}$ for all the cases.

Re_τ	$N_x^f \times N_y^f \times N_z^f$	Δx^{f^+}	Δz^{f^+}	$\Delta y_w^{f^+}$	$\Delta y_c^{f^+}$
180	$720 \times 176 \times 330$	4.7	3.4	0.27	4.4
400	$1388 \times 288 \times 660$	5.4	3.8	0.37	5.9

Table 8: Fluid mesh details.

Re_τ	$N_x^s \times N_y^s \times N_z^s$	Δx^{s^+}	Δz^{s^+}
180	$144 \times 1 \times 66$	4.7	3.4
400	$278 \times 1 \times 132$	5.4	3.8

Table 9: Solid mesh details.

Results

BC	Synthetic rubber ($\times10^3$)		Stainless steel ($\times10^7$)	
	$Re_\tau = 180$	$Re_\tau = 400$	$Re_\tau = 180$	$Re_\tau = 400$
CCCC	0.68	1.65	0.55	2.43
CCCF	0.74	1.84	0.65	3.07
SSSS	3.28	3.27	2.03	9.43

Table 10: Square root of plate-averaged mean square displacement (normalized by δ).

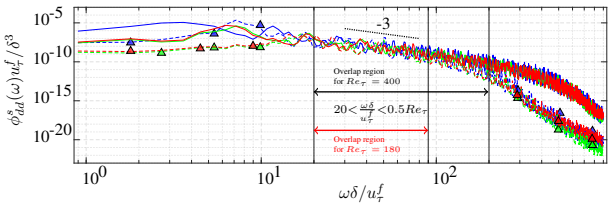

(a)

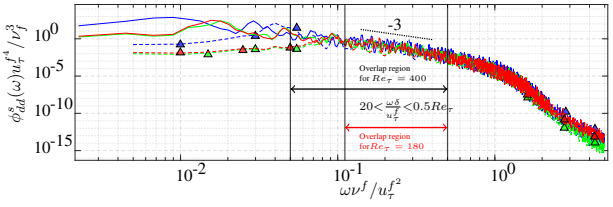

(b)

Figure 15: Plate-averaged displacement spectrum of synthetic rubber plate in (a) outer and (b) inner units. —— (SSSS $Re_\tau = 400$), —— (CCCC $Re_\tau = 400$), —— (CCCF $Re_\tau = 400$), -▲-(SSSS $Re_\tau = 400$), -▲-(CCCC $Re_\tau = 400$), -▲-(CCCF $Re_\tau = 400$).

The square root of the plate-averaged mean-square displacement (refered to as 'displacement rms') is tabulated in table 10 for all the cases. The rms changes by a factor of 2-5 when the boundary condition is changed for fixed plate material and Reynolds number. For a given boundary condition, the change in displacement rms with Reynolds number depends on the plate material; on increasing the Reynolds number from 180 to 400, the rms displacement of the synthetic rubber plate increases by a factor of 1-2 while that of the stainless steel plate increases by a factor of 4-5.

The displacement spectra for the synthetic rubber plate are shown in figures 15a and 15b in outer and inner units, respectively. An overlap region is observed. The spectra in the region $20 < \omega\delta/u_\tau^f < 0.5 (Re_\tau = 180)$ (denoted by $\longleftrightarrow$) collapse with Reynolds number to a similar extent in both outer and inner units. The decay in the spectra is approximately proportional to ω^{-3}. It can be shown that the outer-inner overlap implies a ω^{-3} decay. A proof of this follows. The spectra in the overlap region can be written as follows using both outer and inner scaling.

$$\frac{\phi_{dd}^s(\omega) u_\tau^f}{\delta^3} \approx f_\delta \left(\frac{\omega\delta}{u_\tau^f} \right), \text{ and} \tag{25}$$

$$\frac{\phi_{dd}^s(\omega) u_\tau^{f^4}}{\nu^{f^3}} \approx f_\nu \left(\frac{\omega \nu^f}{u_\tau^{f^2}} \right). \tag{26}$$

Here, f_δ and f_ν are two functions that do not explicitly depend on the Reynolds number. Equate the above two equations and choose $\omega\delta/u_\tau$ and Re_τ as the two independent variables. This yields

$$f_\delta \left(\frac{\omega\delta}{u_\tau^f} \right) \approx f_\nu \left(\frac{\omega\delta}{u_\tau^f} \frac{1}{Re_\tau} \right) \frac{1}{Re_\tau^3}.$$

Partially differentiate w.r.t. Re_τ to obtain

$$-\frac{1}{Re_\tau^4} \left[3 f_\nu \left(\frac{\omega\delta}{u_\tau^f} \frac{1}{Re_\tau} \right) + \frac{\omega\delta}{u_\tau^f} \frac{1}{Re_\tau} f_\nu' \left(\frac{\omega\delta}{u_\tau^f} \frac{1}{Re_\tau} \right) \right] \approx 0.$$

Rearranging yields

$$\frac{\mathrm{d}}{\mathrm{d}\left(\frac{\omega\delta}{u_\tau^f} \frac{1}{Re_\tau} \right)} \left[\left(\frac{\omega\delta}{u_\tau^f} \frac{1}{Re_\tau} \right)^3 f_\nu \left(\frac{\omega\delta}{u_\tau^f} \frac{1}{Re_\tau} \right) \right] \approx 0.$$

This implies

$$f_\nu \left(\frac{\omega \nu^f}{u_\tau^{f^2}} \right) \approx C \left(\frac{\omega \nu^f}{u_\tau^{f^2}} \right)^{-3},$$

where C is the proportionality constant, and therefore, $\phi_{dd}^s(\omega) \approx C\omega^{-3}$.

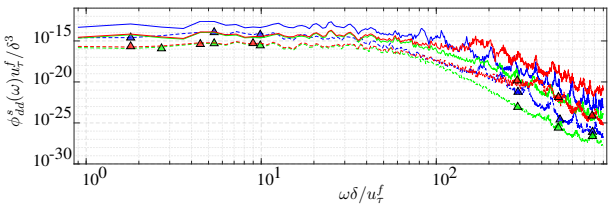

(a)

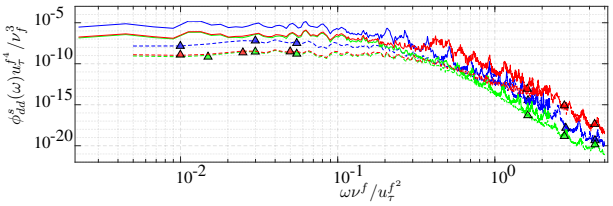

(b)

Figure 16: Plate-averaged displacement spectrum of stainless steel plate in (a) outer and (b) inner units. See caption of figure 15 for the description of lines and symbols.

The stainless steel plate spectra on the other hand does not show such overlap. Their spectra are shown in outer and inner units in figures 16a and 16b, respectively. For an overlap region to exist, we believe that there should be sufficient separation between the time scale of the plate first natural frequency (ω_1) and that of the high-frequency turbulent motion which is set by ν^f and u_τ^f, i.e., $\omega_1 \nu^f / u_\tau^{f^2}$ should be much smaller than one. For the synthetic rubber plates, $\omega_1 \nu^f / u_\tau^{f^2}$ is of order 0.1, while for the stainless steel plates, $\omega_1 \nu^f / u_\tau^{f^2}$ is of order 1. Therefore, the synthetic rubber plates have an overlap region, while the stainless steel plates do not.

The high-frequency portion $(\omega \nu^f / u_\tau^{f^2} > 1)$ of the synthetic rubber plate spectra collapse better with Reynolds number in inner units compared to outer units. See figure 15. This high-frequency collapse does not follow just from the collapse of high-frequency wall-pressure in inner units. This is because u_τ^f changes with Reynolds number, and therefore, the plate thickness in inner units $(h^s u_\tau^f / \nu^f)$ also changes with Reynolds number. Further, the plate spatially filters the wall-pressure based on the modal wavenumber, and therefore, the scaling of the modal wavenumber with Reynolds number also matters. It turns out that the effect of change in plate thickness in inner units gets nullified for mass-proportional damping and that the modal wavenumber scales in inner units. Therefore, the high-frequency displacement spectrum collapses in inner

units. This result can be shown using infinite plate theory. The high-frequency portion of the stainless steel plate also collapses better in inner units. However, the collapse is not as good as that of the synthetic rubber plate.

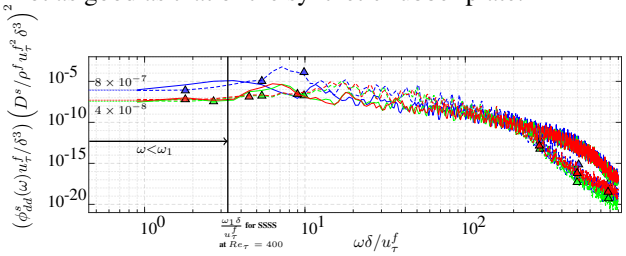

(a)

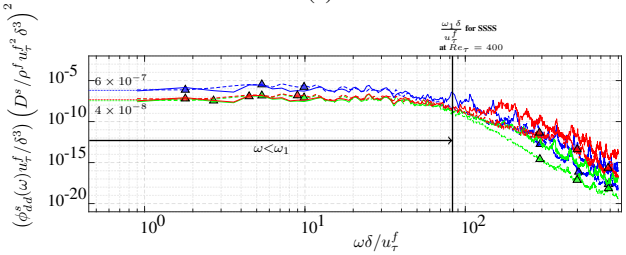

(b)

Figure 17: $\left(\phi^s_{dd}(\omega)u^f_\tau/\delta^3\right)\left(D^s/\rho^f u^{f^2}_\tau\delta^3\right)^2$ v/s $\omega\delta/u^f_\tau$ for (a) synthetic rubber and (b) stainless steel plates. See caption of figure 15 for the description of lines and symbols.

The very low frequency portion (frequencies much smaller than the first natural frequency) of the displacement spectra collapse neither in inner nor in outer units, for both plate materials. It can be shown from Poisson-Kirchoff plate theory that in this region,

$$\left(\frac{\phi^s_{dd}(\omega)u_\tau}{\delta^3}\right)\left(\frac{D^s}{\rho^f u^{f^2}_\tau \delta^3}\right)^2 \text{ v/s } \frac{\omega\delta}{u^f_\tau} \tag{27}$$

collapses with Reynolds number and also with plate material. D^s here is the bending stiffness of the plate. The plate-averaged displacement spectra shown in figure 17 support this result. For a reference first natural frequency, consider that of the simply supported plate for $Re_\tau = 400$ (denoted by vertical black line). For frequencies much smaller than this reference first natural frequency, the collapse with Reynolds number is evident from the figures. For a given boundary condition, the y-intercepts of the synthetic rubber and stainless steel plates are almost coincident. Therefore, the scaling in equation 27 collapses the spectra with both plate material and Reynolds number. Note that the factor D^{s^2} in equation 27 accounts for the change in stiffness with plate material. A similar factor has been previously used by Ciappi et al. (2012). However, they use the plate thickness and wall-pressure convection velocity as the length and velocity scales to account for the Reynolds number dependence. We use the channel half-height and friction velocity to account for the change in Reynolds number.

BC	Synthetic rubber	
	$Re_\tau = 180$	$Re_\tau = 400$
CCCC	16.39	29.75
CCCF	14.85	29.9
SSSS	21.44	27.75

Table 11: Sound pressure level in dB at $r = 50\delta$ below the plate center.

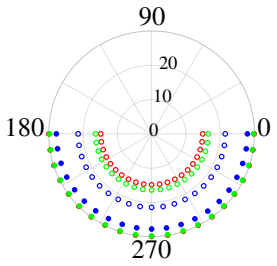

(a)

Figure 18: SPL (in dB) directivity at $r = 50\delta$ for the synthetic rubber plate. • (SSSS $Re_\tau = 400$), • (CCCC $Re_\tau = 400$), • (CCCF $Re_\tau = 400$), ○ (SSSS $Re_\tau = 180$), ○ (CCCC $Re_\tau = 180$), ○ (CCCF $Re_\tau = 180$).

The sound pressure level (SPL) at a radial distance of 50δ below the plate center ($\theta = \phi = 0$) is tabulated in table 11. The statistics of the sound pressure radiated by the stainless steel plates are not shown as they hardly radiate any sound. The boundary condition is found to change the SPL by 2-20dB depending on the plate material and Reynolds number. Note that the sound radiated by the stainless steel plate is very small (negative dB) at these Reynolds numbers. The directivity of SPL at the same radial distance along the plate mid-span ($\phi = 0$) is shown in figure 18. It resembles that of a monopole source for all the cases. This is because, the dominant contribution to the SPL is from the first plate mode, and the ratio of the acoustic wavenumber to the modal wavenumber of the first mode is very small. Therefore, the directivity of the first mode contribution (Hambric and Fahnline, 2007), and hence, the directivity of SPL resembles a monopole source.

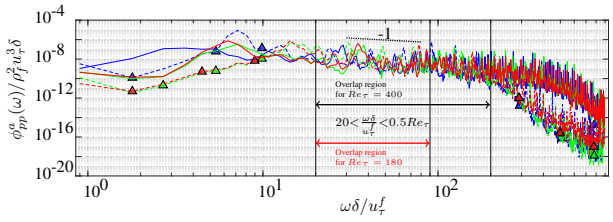

(a)

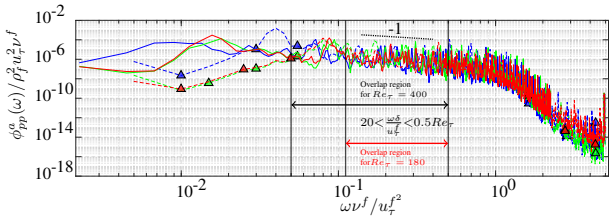

(b)

Figure 19: Acoustic pressure PSD at $r = 50\delta$ below the synthetic rubber plate center in (a) outer and (b) inner units. See caption of figure 15 for the description of lines and symbols.

The acoustic pressure spectra for the synthetic rubber plate computed at a point $r = 50\delta$ below the plate center are shown in figure 19. Figures 19a and 19b is in outer and inner units, respectively. The acoustic pressure spectrum displays an overlap region similar to the displacement spectrum. The $Re_\tau = 180$ overlap region shown by red arrow ($\longleftrightarrow$) collapses with Reynolds number to a similar extent in both outer and inner units. Further, the spectra decay approximately as ω^{-1}. Following a derivation similar to the displacement spectrum, we can analytically show that the outer-inner overlap implies $\phi^a_{pp}(\omega) \approx C\omega^{-1}$.

ONE-WAY COUPLED PLATE EXCITATION SOURCE ANALYSIS

Problem

An elastic plate is embedded in the bottom wall of a turbulent channel. One-way coupling is assumed because the plate deformation and velocity is very small in viscous units. The contribution of shear-stress fluctuations is neglected because the plate is thin. For thin plates, the bending stiffness is much smaller (scales as cube of the plate thickness) than the shear modulus. Therefore, the bending deformation would be much larger than shear deformation. The problem domain and dimensions are the same as that in the previous section; except the acoustic domain is omitted. The plate is clamped on all four sides. The top and bottom sides are free. The non-dimensional Young's modulus, density, and Poisson's ratio of the plate are tabulated in table 12. The mass proportional damping coefficient is set such that the loss factor is 0.05 at the natural frequency (same as in the previous section). The friction Reynolds numbers considered are 180 and 400.

Young's modulus ($E/\left(\rho_f u_\tau^2\right)$)	6.88×10^9
Poisson ratio (ν_s)	0.4
Solid density (ρ_s/ρ_f)	1.17×10^3

Table 12: Non-dimensional properties of the plate.

Method

The main idea behind this method is to express the plate-averaged displacement spectrum as a double integral of a cross-spectral density using theory, and then to compute this cross-spectral density by postprocessing the channel DNS velocity field. This method is an extension of Anantharamu and Mahesh (2020) which is a similar method to analyze the wall-pressure sources instead.

Denote the plate-averaged displacement spectrum by $\phi^a_{dd}(\omega)$. By using the pressure fluctuation Poisson equation and the modal decomposition of the plate, it can be shown that

$$\phi^a_{dd}(\omega) = \int_{-\delta}^{+\delta}\int_{-\delta}^{+\delta} \Gamma^a(r,s,\omega), \mathrm{d}r\, \mathrm{d}s, \tag{28}$$

where, δ is the half-channel height, $\Gamma^a(r,s,\omega)$ is a cross-spectral density whose expression can be shown to be

$$\Gamma^a(r,s,\omega) = \frac{1}{\rho^s L_y^s A_p} \iint_{-\infty}^{+\infty} G^*(-\delta,r,k)G(-\delta,s,k)\varphi_{ff}(r,s,k_1,k_3,\omega) \left(\sum_{j=1}^{\infty} |S_j(k_1,k_3)|^2 |H_j(\omega)|^2\right) \mathrm{d}k_1\, \mathrm{d}k_3. \tag{29}$$

Here, ρ^s, L_y^s, and A_p are the density, thickness, and area of the plate, respectively, k is the magnitude of the wave vector (k_1, k_3), G is the Green's function, φ_{ff} is the four-dimensional cross-spectral density of the right hand side of the Poisson equation for the pressure fluctuation, j is the index of the plate mode, S_j is the finite-domain Fourier transform of the j^{th} plate mode shape, and $|H_j|^2$ is the transfer function of the j^{th} plate mode. We refer to $\Gamma^a(r,s,\omega)$ as the net displacement source cross-spectral density.

To identify the decorrelated features, spectral POD of the cross-spectral density $\Gamma^a(r,s,\omega)$ is performed as follows. Solve the eigenvalue problem:

$$\int_{-\delta}^{+\delta} \Gamma^a(r,s,\omega)\, \bar{\Phi}_j(s,\omega)\, \mathrm{d}s = \lambda_j(\omega) \left(\left(-(1-\beta)\frac{\partial^2}{\partial y^2} + \beta\right)\bar{\Phi}_j\right)(r,\omega), \tag{30}$$

where β is a small value satisfying $0 < \beta \leq 1$. The spectral POD modes are Φ_j which relates to the eigenfunction $\bar{\Phi}_j$ through the relation $\Phi_j = \left(-(1-\beta)\frac{\partial^2}{\partial y^2} + \beta\right)\bar{\Phi}_j$. The spectral POD eigenvalues are $\lambda_j(\omega)$. These spectral POD modes and eigenvalues relate to the cross-spectral density as

$$\Gamma^a(r,s,\omega) = \sum_{j=1}^{\infty} \lambda_j(\omega)\Phi_j(r,\omega)\Phi_j^*(s,\omega). \tag{31}$$

The difference between the above version of spectral POD and the most common version (Lumley, 2007; Towne et al., 2018) of spectral POD is in the inner product used to enforce the orthogonality of the eigenfunctions. In the above version, the orthogonality is enforced in the inner product

$$\int_{-\delta}^{+\delta} \left(\left(-(1-\beta)\frac{\partial^2}{\partial y^2} + \beta\right)\bar{\Phi}_i\right)\bar{\Phi}_j^* \,\mathrm{dy} = \delta_{ij}, \tag{32}$$

while in the most common version, the orthogonality is enforced in the L^2 inner product. The reason for not using the L^2 inner product is because the L^2 inner-product isolates the dominant source to the integral $\int_{-\delta}^{+\delta} \Gamma^a(r,r,\omega)\,\mathrm{dr}$ and not the plate-average displacement spectrum. On the other hand, it turns out that, for a small enough value of β, the inner product in equation 32 isolates the source that contributes the most to the plate-averaged displacement spectrum. Therefore, we use the inner product in equation 32 instead of the commonly used L^2 inner product.

Implementation

The net displacement source cross-spectral density Γ^a is computed using 80TB of $Re_\tau = 400$ and 12TB of $Re_\tau = 180$ DNS velocity data. This computation is both memory and I/O intensive. A special parallel tool was developed for this purpose. It uses a low memory consuming streaming method to compute Γ^a. Direct computation of the four-dimensional cross-spectral density φ_{ff} requires around 1000TB of RAM for $Re_\tau = 400$ case, and is therefore prohibitively memory intensive. To perform the summation in equation 29, 50 modes are used. It turns out that the first 50 modes are sufficient to analyze the sources up to $\omega\delta/u_\tau^f = 500$.

The 3D DNS velocity is sampled with a temporal resolution of $\Delta t u_\tau/\delta = 3.5 \times 10^{-3}$ for both Reynolds numbers. A total of $20\delta/u_\tau$ and $23\delta/u_\tau$ time units are used for $Re_\tau = 180$ and 400, respectively. In each FFT chunk, we use 2000 samples which leads to a frequency resolution of $\Delta\omega\delta/u_\tau = 2\pi/7$. To reduce the spectral leakage and to increase the statistical convergence, we use Hanning window with 75% overlap. Further, to account for the reduction in the spectral level after windowing, we multiply the estimated CSD by a factor of $8/3$ (Bendat and Piersol, 2011).

Results

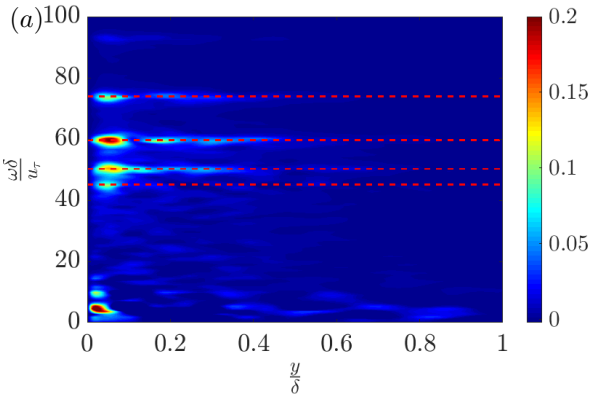

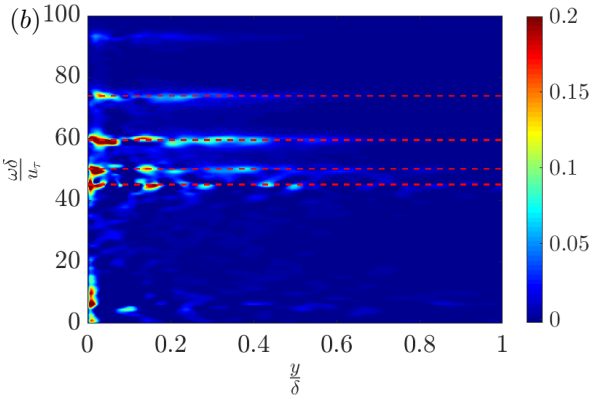

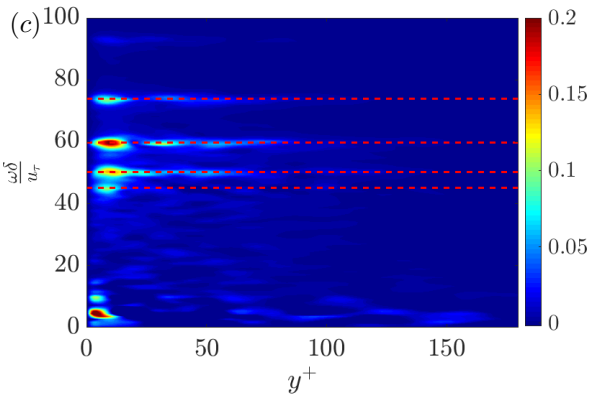

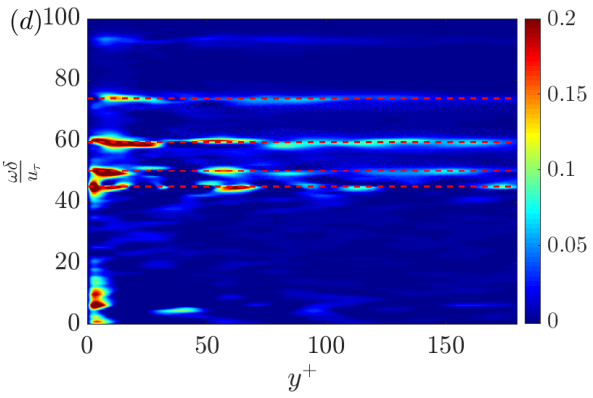

Figure 20: Real part of the normalized wall displacement-net displacement source CSD $\frac{Re(\Psi_a(y,\omega))}{\int_{-\infty}^{+\infty}\int_{-1}^{+1}\Psi_a(y,\omega\delta)\,\mathrm{dy}/\delta\,\mathrm{d}\omega\delta/\mathrm{u}_\tau}$. The wall-normal distance is in outer units in figures (a) and (b), and is in inner units in figures (c) and (d). Figures (a) and (c) are for $Re_\tau = 180$, and figures (b) and (d) are for $Re_\tau = 400$. In all the figures, the contours are 100 equally spaced values between -0.002 and 0.2. Horizontal dashed red lines denote the first four natural frequencies of the plate.

Range	$Re_\tau = 180$	$Re_\tau = 400$
$0 < y^+ < 30$	0.52	0.34
$30 < y^+ < 0.2Re_\tau$	0.06	0.17
$0.2 < y/\delta < 1$	0.41	0.49

Table 13: Fractional contribution of different wall-normal regions to the plate-averaged mean square displacement.

Figure 20 shows the real part of the plate-averaged wall displacement-net displacement source CSD $\Psi^a(y,\omega)$ which relates to Γ^a as $\Psi^a(y,\omega) = \int_{-\delta}^{+\delta}\Gamma^a(y,s,\omega)\,\mathrm{ds}$. Ψ^a gives the contribution of the correlation with the sources at distance y from the wall to the plate-averaged displacement spectrum at each frequency ω. Note that integrating Ψ^a along y gives the plate averaged displacement spectrum. In figures 20a and b, the wall-normal distance is in outer units. In figures 20c and d, the wall-normal distance is in inner units. Figures 20a and c are for $Re_\tau = 180$, and figures 20b and d are for $Re_\tau = 400$. In all figures, the frequency ordinates of the four horizontal dashed red lines are the first four natural frequencies of the plate. From a visual inspection of the contours in figure 20, we see that the fluid sources around the natural frequencies are the dominant contributors to the structural response. This dominant contribution peaks close to the wall in the buffer region (figures 20c and d), and extends to the outer region of the channel up to $y/\delta \approx 0.75$ (figures 20c and d).

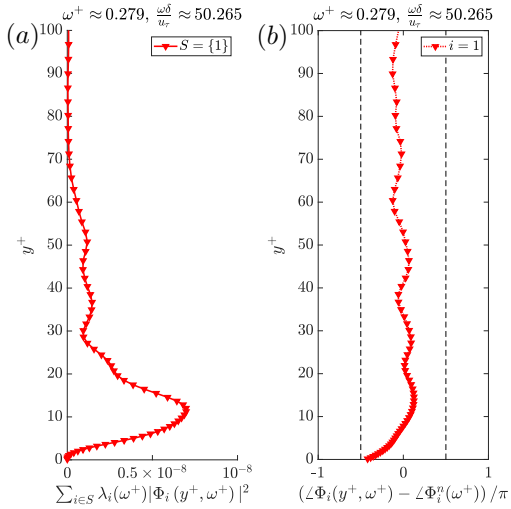

Figure 21: (a) Envelope and (b) phase of the dominant spectral POD mode for $Re_\tau = 180$ for the second natural frequency.

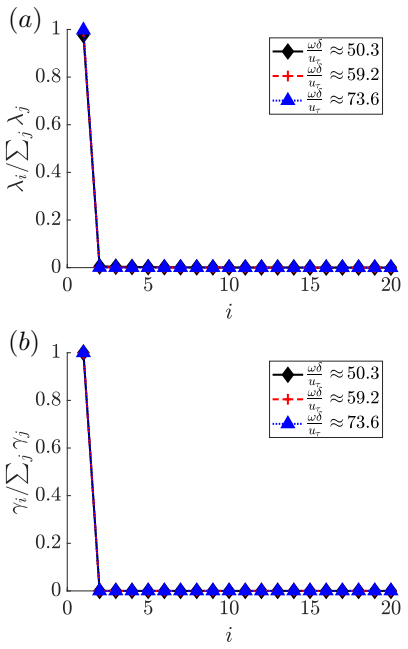

Figure 22: (a) Spectral POD eigenvalues and (b) fractional contribution of each mode to the plate-averaged displacement PSD at $Re_\tau = 180$.

Table 13 shows the fractional contribution of sources in the inner, overlap, and outer region of the channel to the plate-averaged mean square displacement. These values are computed by partially integrating $\Psi^a(y,\omega)$. The contribution of the outer and overlap region increases with

Reynolds numbers while the inner region's contribution decreases. Further, the combined contribution of the overlap and outer regions to the plate response is comparable to that of the buffer region for $Re_\tau = 180$ and exceeds the buffer region contribution for $Re_\tau = 400$.

For brevity, only the $Re_\tau = 180$ spectral POD results are presented here. The parameter β is set to 0.01 for all the cases. For a discussion on the choice of β, we refer the reader to Anantharamu and Mahesh (2021). The spectral POD eigenvalues and the contribution of each eigenvalue to the plate-averaged displacement spectrum are shown in figures 22a and 22b, respectively, for the second, third, and fourth natural frequencies of the plate. The first spectral POD mode is the most dominant and accounts for almost the entire displacement spectrum. Therefore, the inner-product in equation 32 is successful in isolating the dominant decorrelated plate excitation feature. The envelope and phase of this dominant feature is shown in figure 21 for the second natural frequency. The envelope peaks in the buffer layer and its width extends up to the outer layer similar to the contours of Ψ^a. The phase lies between $-\pi/2$ and $+\pi/2$. This implies a constructive interference of the contributions from the different wall-parallel planes. In the sub-optimal modes, this contribution interferes destructively resulting in a net zero contribution (not shown). Therefore, the mechanism responsible for the dominant source is the constructive interference of the contributions from the different wall-normal locations.

SUMMARY

In summary, this paper discusses

- the development of numerical methods to simulate turbulent fluid-structure interaction problems using DNS/LES,
- some new findings in the context of wall-pressure induced plate vibration and sound radiation problem using one-way coupled DNS, and
- a data-intensive method to identify the spatial and spectral features of the turbulent sources that excite a plate embedded in the bottom wall of a turbulent channel.

Extensions to our in-house solver MPCUGLES to perform accurate LES/DNS in curved and deforming meshes are discussed. These extensions are developed in the context of a canonical turbulent FSI problem: response of an incompressible viscoelastic wall in an incompressible turbulent channel. Numerical experiments demonstrate the second-order accuracy, and stability of the computed solution even in the presence of extremely skewed and curved elements which might arise while simulating deforming geometries.

The development of a method to couple the fluid and solid solutions is discussed in the context of the same FSI problem. This method allows for the simultaneous execution of the fluid and solid solvers, and hence, is a parallel coupling approach. It uses the Steklov-Poincare operator for this feature. Steklov-Poincare operator-based methods were previously thought to be possible only for finite element discretizations in the fluid and solid domain. This development is the first to extend its applicability to a finite volume discretization in the fluid and a finite element discretization in the solid. Some preliminary results of the two-way coupled problem are presented.

The dependence of wall-pressure fluctuation induced plate vibration and far-field sound on plate boundary condition, plate material, and Reynolds number is studied using one-way coupled DNS. The plate boundary condition has a non-negligible impact on displacement rms (factor of 4-5), and far-field SPL (2-20dB). For frequencies much smaller than the plate first natural frequency, $(\phi^s_{dd}(\omega)u_\tau/\delta^3)\left(D^s/(\rho^f {u^f_\tau}^2 \delta^3)\right)^2$ v/s $\omega\delta/u^f_\tau$ is found to collapse with both plate material and Reynolds number. The displacement spectra of the synthetic rubber plate show an overlap region, while that of the stainless steel plate do not. In this overlap region, the displacement and spectra decays as ω^{-3}. This trend is observed in our simulations.

A method to quantitatively analyse the turbulent fluid sources that excite a plate embedded in the bottom wall of a turbulent channel is discussed. Around 100TB of $Re_\tau = 180$ and 400 channel DNS data is processed for this analysis. At these Reynolds numbers, the intensity of the dominant contribution is found to peak in the buffer region, and the width of this intensity extends to the outer region of the channel. The combined contribution from the sources in the outer and overlap region to the mean-square displacement is found to increase with Reynolds number while the contribution from the inner region sources is found to decrease. Spectral POD is used to isolate the dominant decorrelated contribution to the plate excitation into the first spectral POD mode. From the phase of this dominant mode, it is found that the contribution from the different wall-parallel planes interfere constructively. On the other hand, the contribution from the different wall-normal regions for the remaining modes interfere destructively resulting in a zero net contribution.

ACKNOWLEDGEMENTS

This work is supported by the United States Office of Naval Research (ONR) under grant N00014-17-1-2939 with Dr. Ki-Han Kim as the technical monitor. The computations were made possible through computing

resources provided by the US Army Engineer Research and Development Center (ERDC) in Vicksburg, Mississippi on the Cray X6, Copper and Onyx of the High Performance Computing Modernization Program. Computing resources provided by the Minnesota Supercomputing Institute (MSI) are acknowledged.

REFERENCES

Anantharamu, Sreevatsa and Mahesh, Krishnan. "Analysis of wall-pressure fluctuation sources from direct numerical simulation of turbulent channel flow". *Journal of Fluid Mechanics*, 898, 2020.

Anantharamu, Sreevatsa and Mahesh, Krishnan. "Response of a plate in turbulent channel flow: Analysis of fluid–solid coupling". *Journal of Fluids and Structures*, 100:103173, 2021.

Arnold, Douglas N, Boffi, Daniele, Falk, Richard S, and Gastaldi, Lucia. "Finite element approximation on quadrilateral meshes". *Communications in Numerical Methods in Engineering*, 17(11):805–812, 2001.

Bendat, J. S. and Piersol, A. G. *Random data: analysis and measurement procedures*. John Wiley & Sons, 2011.

Bernardini, M., Pirozzoli, S., Quadrio, M., and Orlandi, P. "Turbulent channel flow simulations in convecting reference frames". *J. Comp. Phys.*, 232:1–6, 2013.

Blake, W. K. *Mechanics of Flow-Induced Sound and Vibration, Volume 1 and 2*. Academic Press, 2017.

Bull, M. K. "Wall-pressure fluctuations associated with subsonic turbulent boundary layer flow". *Journal of Fluid Mechanics*, 28(4):719–754, 1967.

Chase, D. M. "Modeling the wavevector-frequency spectrum of turbulent boundary layer wall pressure". *Journal of Sound and Vibration*, 70(1):29–67, 1980.

Chase, DM. "The character of the turbulent wall pressure spectrum at subconvective wavenumbers and a suggested comprehensive model". *Journal of Sound and Vibration*, 112(1):125–147, 1987.

Ciappi, E., Magionesi, F., De Rosa, S., and Franco, F. "Analysis of the scaling laws for the turbulence driven panel responses". *Journal of Fluids and Structures*, 32: 90–103, 2012.

Corcos, G. M. "The structure of the turbulent pressure field in boundary-layer flows". *J. Fluid Mech.*, 18: 353–378, 1964.

De Rosa, S and Franco, F. "Exact and numerical responses of a plate under a turbulent boundary layer excitation". *Journal of Fluids and Structures*, 24(2): 212–230, 2008.

Degroote, Joris, Bathe, Klaus-Jürgen, and Vierendeels, Jan. "Performance of a new partitioned procedure versus a monolithic procedure in fluid–structure interaction". *Computers & Structures*, 87(11-12): 793–801, 2009.

Deparis, Simone, Discacciati, Marco, Fourestey, Gilles, and Quarteroni, Alfio. "Fluid–structure algorithms based on steklov–poincaré operators". *Computer Methods in Applied Mechanics and Engineering*, 195 (41-43):5797–5812, 2006.

Donea, Jean, Huerta, Antonio, Ponthot, Jean-Philippe, and Rodríguez-Ferran, Antonio. "Arbitrary l agrangian–e ulerian methods". *Encyclopedia of Computational Mechanics Second Edition*, pages 1–23, 2017.

Esmailzadeh, Mitra, Lakis, Aouni A, Thomas, Marc, and Marcouiller, L. "Prediction of the response of a thin structure subjected to a turbulent boundary-layer-induced random pressure field". *Journal of sound and vibration*, 328(1-2):109–128, 2009.

Farhat, Charbel, Lesoinne, Michel, and Maman, Nathan. "Mixed explicit/implicit time integration of coupled aeroelastic problems: Three-field formulation, geometric conservation and distributed solution". *International Journal for Numerical Methods in Fluids*, 21(10):807–835, 1995.

Farhat, Charbel, Van der Zee, Kristoffer G, and Geuzaine, Philippe. "Provably second-order time-accurate loosely-coupled solution algorithms for transient nonlinear computational aeroelasticity". *Computer methods in applied mechanics and engineering*, 195 (17-18):1973–2001, 2006.

Goody, M. "Empirical spectral model of surface pressure fluctuations". *AIAA Journal*, 42(9):1788–1794, 2004.

Hambric, S. A. and Fahnline, J. B. "Structural acoustics tutorial—part 2: sound—structure interaction". *Acoust. Today*, 3(2):9, 2007.

Hambric, S. A., Hwang, Y. F., and Bonness, W. K. "Vibrations of plates with clamped and free edges excited by low-speed turbulent boundary layer flow". *Journal of Fluids and Structures*, 19(1):93–110, 2004.

Hughes, Thomas JR, Engel, Gerald, Mazzei, Luca, and Larson, Mats G. "The continuous galerkin method is locally conservative". *Journal of Computational Physics*, 163(2):467–488, 2000.

Hwang, Y. F. and Maidanik, G. "A wavenumber analysis of the coupling of a structural mode and flow turbulence". *Journal of Sound and Vibration*, 142(1): 135–152, 1990.

Jang, Hyunchul, Verma, Aman, and Mahesh, Krishnan. "Predicting unsteady loads in marine propulsor crashback using large eddy simulation". *International Journal of Rotating Machinery*, 2012, 2012.

Kumar, Praveen and Mahesh, Krishnan. "Large eddy simulation of propeller wake instabilities". *Journal of Fluid Mechanics*, 814:361–396, 2017.

Küttler, Ulrich and Wall, Wolfgang A. "Fixed-point fluid–structure interaction solvers with dynamic relaxation". *Computational mechanics*, 43(1):61–72, 2008.

Leissa, A. W. "Vibration of plates". Technical report, Ohio State University, Columbus, Ohio, 1969.

Li, Xiaoye S and Demmel, James W. "Superlu_dist: A scalable distributed-memory sparse direct solver for unsymmetric linear systems". *ACM Transactions on Mathematical Software (TOMS)*, 29(2):110–140, 2003.

Lumley, J. L. *Stochastic tools in turbulence*. Courier Corporation, 2007.

Mahesh, K., Constantinescu, G., and Moin, P. "A numerical method for large-eddy simulation in complex geometries". *Journal of Computational Physics*, 197(1):215–240, 2004.

Mehl, Miriam, Uekermann, Benjamin, Bijl, Hester, Blom, David, Gatzhammer, Bernhard, and Van Zuijlen, Alexander. "Parallel coupling numerics for partitioned fluid–structure interaction simulations". *Computers & Mathematics with Applications*, 71(4):869–891, 2016.

Mellen, RH. "Wave-vector filter analysis of turbulent flow". *The Journal of the Acoustical Society of America*, 95(3):1671–1673, 1994.

Mittal, Rajat and Moin, Parviz. "Suitability of upwind-biased finite difference schemes for large-eddy simulation of turbulent flows". *AIAA journal*, 35(8): 1415–1417, 1997.

Nobile, Fabio. "Numerical approximation of fluid-structure interaction problems with application to haemodynamics". Technical report, EPFL, 2001.

Persson, P-O, Bonet, Javier, and Peraire, Jaime. "Discontinuous galerkin solution of the navier–stokes equations on deformable domains". *Computer Methods in Applied Mechanics and Engineering*, 198(17-20): 1585–1595, 2009.

Piperno, Serge and Farhat, Charbel. "Partitioned procedures for the transient solution of coupled aeroelastic problems–part ii: energy transfer analysis and three-dimensional applications". *Computer methods in applied mechanics and engineering*, 190 (24-25):3147–3170, 2001.

Piperno, Serge, Farhat, Charbel, and Larrouturou, Bernard. "Partitioned procedures for the transient solution of coupled aroelastic problems part i: Model problem, theory and two-dimensional application". *Computer methods in applied mechanics and engineering*, 124(1-2):79–112, 1995.

Quarteroni, Alfio and Valli, Alberto. "Theory and application of steklov-poincaré operators for boundary-value problems". In *Applied and Industrial Mathematics*, pages 179–203. Springer, 1991.

Saad, Yousef. *Iterative methods for sparse linear systems*. SIAM, 2003.

Silvester, David, Elman, Howard, Kay, David, and Wathen, Andrew. "Efficient preconditioning of the linearized navier–stokes equations for incompressible flow". *Journal of Computational and Applied Mathematics*, 128(1-2):261–279, 2001.

Smol'Iakov, A. V. and Tkachenko, V. M. "Models of a field of pseudoacoustic turbulent wall pressures and experimental data". *Akusticheskii Zhurnal*, 37: 1199–1207, 1991.

Thomas, PD and Lombard, CK. "Geometric conservation law and its application to flow computations on moving grids". *AIAA journal*, 17(10):1030–1037, 1979.

Towne, Aaron, Schmidt, Oliver T, and Colonius, Tim. "Spectral proper orthogonal decomposition and its relationship to dynamic mode decomposition and resolvent analysis". *Journal of Fluid Mechanics*, 847: 821–867, 2018.

Trilinos Project Team, The. *The Trilinos Project Website*.

Zienkiewicz, Olek C and Taylor, Robert L. *The finite element method for solid and structural mechanics*. Elsevier, 2005.